

# Unresolved stellar companions with *Gaia* DR2 astrometry

Vasily Belokurov<sup>1\*</sup>, Zephyr Penoyre<sup>1</sup>, Semyeong Oh<sup>1</sup>, Giuliano Iorio<sup>1,2</sup>, Simon Hodgkin<sup>1</sup>, N. Wyn Evans<sup>1</sup>, Andrew Everall<sup>1</sup>, Sergey E. Koposov<sup>3,1,4</sup>, Christopher A. Tout<sup>1</sup>, Robert Izzard<sup>5</sup>, Cathie J. Clarke<sup>1</sup> and Anthony G. A. Brown<sup>6</sup>

<sup>1</sup>*Institute of Astronomy, Madingley Rd, Cambridge, CB3 0HA*

<sup>2</sup>*Dipartimento di Fisica e Astronomia G. Galilei, Università di Padova, vicolo dell'Osservatorio 3, 35122 PD, Italy*

<sup>3</sup>*McWilliams Center for Cosmology, Carnegie Mellon University, 5000 Forbes Ave, 15213, USA*

<sup>4</sup>*Kavli Institute for Cosmology, University of Cambridge, Madingley Road, Cambridge CB3 0HA, UK*

<sup>5</sup>*Astrophysics Research Group, University of Surrey, Guildford, Surrey, GU2 7XH*

<sup>6</sup>*Leiden Observatory, Leiden University, Niels Bohrweg 2, 2333 CA Leiden, The Netherlands*

13 March 2020

## ABSTRACT

For stars with unresolved companions, motions of the centre of light and that of mass decouple, causing a single-source astrometric model to perform poorly. We show that such stars can be easily detected with the reduced  $\chi^2$  statistic, or RUWE, provided as part of *Gaia* DR2. We convert RUWE into the amplitude of the image centroid wobble, which, if scaled by the source distance, is proportional to the physical separation between companions (for periods up to several years). We test this idea on a sample of known spectroscopic binaries and demonstrate that the amplitude of the centroid perturbation scales with the binary period and the mass ratio as expected. We apply this technique to the *Gaia* DR2 data and show how the binary fraction evolves across the Hertzsprung–Russell diagram. The observed incidence of unresolved companions is high for massive young stars and drops steadily with stellar mass, reaching its lowest levels for white dwarfs. We highlight the elevated binary fraction for the nearby Blue Stragglers and Blue Horizontal Branch stars. We also illustrate how unresolved hierarchical triples inflate the relative velocity signal in wide binaries. Finally, we point out a hint of evidence for the existence of additional companions to the hosts of extrasolar hot jupiters.

**Key words:** stars: evolution – stars: binaries – stars: Hertzsprung–Russell

## 1 INTRODUCTION

A star’s path on the sky is often wiggled, but not always due to its parallax. Unresolved stellar companions induce photocentre wobble giving us a chance to detect binary systems via astrometry. This was first demonstrated almost a century ago (see Reuyl 1936; Lipincott 1955). Better still, the motion of the centre of light can be straightforwardly interpreted, placing constraints on the properties of the unseen companion (see van de Kamp 1975). Space-based astrometric missions such as *Hipparcos* (Perryman et al. 1997) and *Gaia* (Perryman et al. 2001; Gaia Collaboration et al. 2016) have offered a much improved chance of discovering small wobbles in the stellar motion due to multiplicity. Inspired by this, the community has understandably focused on stellar companions that are tricky to observe otherwise such as exosolar planets (Lattanzi et al. 1997; Sozzetti et al. 2001; Casertano et al. 2008; Perryman et al. 2014) and dark remnants such as black holes (Mashian &

Loeb 2017; Breivik et al. 2017; Kinugawa & Yamaguchi 2018; Yalınwıch et al. 2018; Yamaguchi et al. 2018; Andrews et al. 2019).

Constraining the statistics of opposite ends of the companion mass function as well as everything in between is crucial to our understanding of stellar multiplicity which forms one of the foundations of astrophysics. As a channel to study fragmentation processes at the birth sites, it informs the theory of star formation (see e.g. Bate et al. 1995, 2003; McKee & Ostriker 2007). At high redshifts, multiplicity of the first stellar systems stipulates how the mass is apportioned between the Population III stars and thus controls the ionizing radiation and metal enrichment, which in turn define the subsequent growth of structure in the Universe (e.g. Barkana & Loeb 2001; Abel et al. 2002; Heger & Woosley 2002; Stacy et al. 2010; Stanway et al. 2016). Supernovae of type Ia are a product of a binary star evolution (Whelan & Iben 1973; Tutukov & Yungelson 1981; Iben & Tutukov 1984; Webbink 1984; Maoz et al. 2014), and several other sub-types are suspected to be (Podsiadlowski et al. 1993; Smartt et al. 2009; Smith et al. 2011). Supernovae are not the only extremely high energy events linked to the binary star evolution. High mass binaries also serve as progen-

\* E-mail: vasily@ast.cam.ac.uk

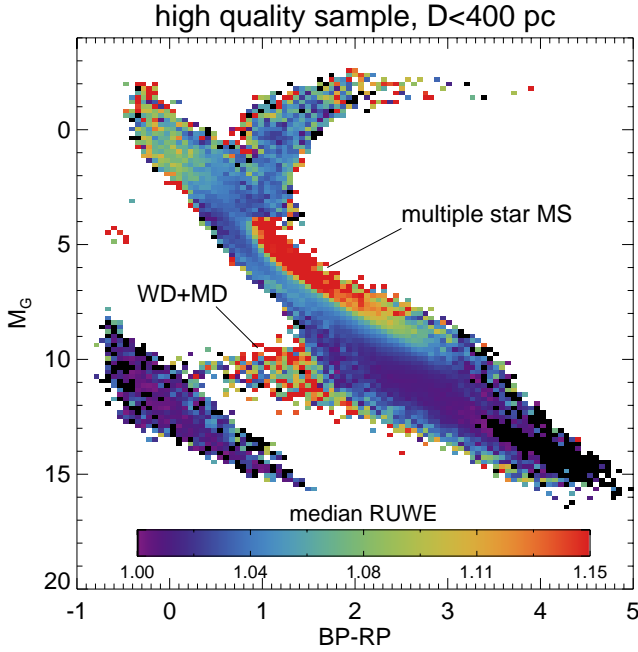


**Figure 1.** Median RUWE as a function of extinction-corrected color and absolute magnitude for  $\sim 4,000,000$  stars selected using the criteria listed in Equation 6 but with a distance cut  $D < 400$  pc. Running parallel to and above the single-star Main Sequence is the photometric binary MS which has a notably elevated median RUWE. Another region with a clear RUWE excess is the sequence of white dwarf-M dwarf binaries at  $10 < G < 12$  and  $BP-RP < 2$ . Clear systematic and predictable patterns of RUWE variation support the idea of using reduced  $\chi^2$  to test the presence of unresolved companions to *Gaia* stars.

itors for gamma-ray bursts (see Narayan et al. 1992; Berger 2014) and gravitational waves (see Belczynski et al. 2002; Abbott et al. 2016), the two events that in some cases are also predicted to occur (nearly) simultaneously in the same system (Blinnikov et al. 1984; Abbott et al. 2017). Finally, binaries, even in very small numbers, control the dynamical evolution of dense stellar systems (Heggie 1975).

An impressive variety of observational techniques has been used so far to probe stellar multiplicity across a wide range of companion masses and separations. These include photometry, spectroscopy, eclipses, common proper motions, adaptive optics and interferometry (see e.g. Moe & Di Stefano 2017). An early example of a comprehensive attempt to calculate the multiplicity frequency of Solar type stars, including a correction for observational biases, was reported by Abt & Levy (1976) and updated by Duquennoy & Mayor (1991). They used a sample of less than two hundred stars. Some twenty years later, the analysis was brought up to date with a sample of about 500 stars (Raghavan et al. 2010) this time taking advantage of the astrometric distances provided by *Hipparcos*. These studies not only provided the first robust overall estimates of the percentages of double, triple and higher-multiple systems but also detected a clear evolution of the binary fraction with stellar mass. It is now established that O and B stars are much more likely to reside in a pair compared to stars further down the Main Sequence (see Garmany et al. 1980; Raghavan et al. 2010; Sana et al. 2012; Duchêne & Kraus 2013; Moe & Di Stefano 2017). With the advent of wide-angle highly multiplexed spectroscopic surveys, the sizes of stellar samples available for the studies of binarity grew by

several orders of magnitude (see e.g. Badenes & Maoz 2012; Hettinger et al. 2015; Badenes et al. 2018; Price-Whelan et al. 2018; El-Badry et al. 2018). Thanks to the increase in the sample size, trends in the stellar multiplicity that had previously been hinted at are now getting firmly established (see e.g. Price-Whelan & Goodman 2018; Moe et al. 2019; Price-Whelan et al. 2020; Merle et al. 2020).

Astrometric surveys in general, and *Gaia* in particular, provide new, complimentary ways of detecting stellar companions. As pointed out by Luyten (1971), wide separation binaries can be straightforwardly identified as pairs of stars with similar distances and similar proper motions (see Oh et al. 2017; Andrews et al. 2017; El-Badry & Rix 2018a, for applications to the *Gaia* data). Faint or unresolved companions can induce a shift of the barycentre with respect to the photocentre which can be detected when proper motion estimates from two or more epochs are compared in a method known as the proper motion anomaly (PMA, see e.g. Bessel 1844; Brandt 2018; Kervella et al. 2019a,b). Here we explore a regime complimentary to the proper motion anomaly. Similar to the PMA method, we study cases where the motions of the centre of light and the centre of mass are sufficiently different. If the binary period is smaller than the *Gaia*'s temporal baseline then the additional centroid perturbation is non-linear and cannot be absorbed into the proper motion so the goodness of fit is decreased. This can be detected as an excess in reduced  $\chi^2$ .

## 2 PHOTOCENTRE WOBBLE WITH RUWE

Our working premise is that the amplitude of the photocentre perturbation due to binary orbital motion can be gauged from the reduced  $\chi^2$  of the single-source astrometric fit<sup>1</sup>. In practice, we use a closely related quantity, namely RUWE or  $\rho$ , the re-normalised unit weight error (see e.g. Lindegren et al. 2018). The re-normalisation was required after it was noticed that the peak of the reduced  $\chi^2$  distribution depended on the source colour and apparent magnitude. Here, we assume that the re-normalisation (as described in Lindegren et al. 2018) corrects the bulk of the *Gaia* DR2 systematics so that  $\rho^2$  closely approximates true reduced  $\chi^2$

$$\rho^2 \approx \chi_\nu^2 = \frac{1}{\nu} \sum_{i=1}^N \frac{R_i^2}{\sigma_i^2}. \quad (1)$$

Here,  $\nu = N - 5$  is the number of degrees of freedom, for the single-source 5-parameter model used in *Gaia* DR2. The number of observations  $N = \text{astrometric\_n\_good\_obs\_al}$ .  $R_i$  and  $\sigma_i$  are the along-scan data-model residuals and the corresponding centroiding errors of  $i$ -th measurement of the given star. If the source is an unresolved binary system, the motions of the centre of mass and the centre of light separate. The barycentre motion is still adequately describable with a 5-parameter model, but the centre of light trajectory now contains an additional component due to the binary orbital motion. We therefore expect that unresolved binaries should yield poorer goodness-of-fit statistics, e.g. RUWE.

Figure 1 shows the median RUWE value as a function of the position on the Hertzsprung-Russel Diagram spanned by

<sup>1</sup> Note however, that, as we discuss below and demonstrate in detail in Penoyre et al (submitted), reduced  $\chi^2$  does not always correlate with the amplitude of the centroid perturbation, as some of the centroid motion can be soaked up in parallax or proper motion (creating the so-called proper motion anomaly).

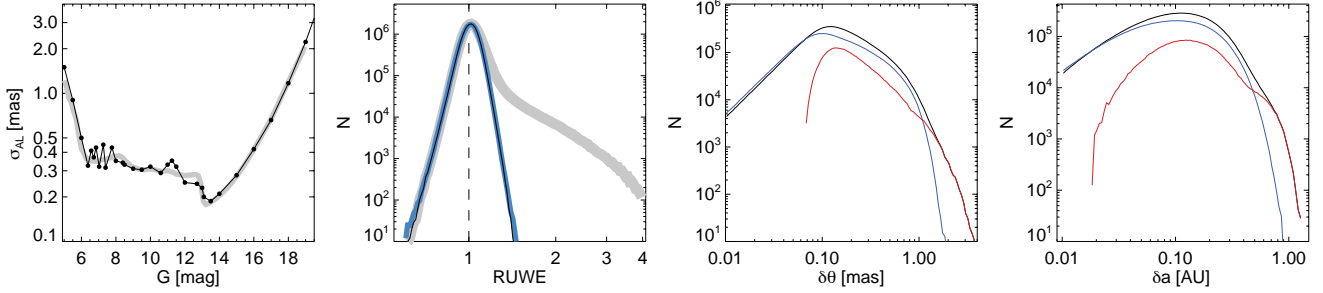


**Figure 2.** Astrometric properties of stars satisfying the selection in Equation 6. *1st panel:* Black filled circles and line show the along-scan error  $\sigma_{AL}$  as given by the blue line in Lindegren et al. (2018). Grey curve corresponds to  $0.53\sqrt{N}\sigma_{\varpi}$  (see text for details). *2nd panel:* Thick grey line gives the Gaia DR2 RUWE distribution for the selected sources. Thin black line corresponds to the RUWE distribution reflected around the peak at  $\rho_{peak} = 1.012$  which represents the properties of the sources without significant centroid perturbation. Blue thick curve is our model of this symmetric distribution of unaffected sources (see text for details). *3rd panel:* Distribution of  $\delta\theta$  for a subset of Gaia DR2 sources calculated using Equation 2 (black line) together with our estimate of the background (blue line), i.e. the objects with values of RUWE close to 1 upscattered by high centroiding errors. Red curve, the difference of the two distributions, shows a clear excess of sources with noticeable centroid wobble above  $\delta\theta \sim 0.1$  mas. *4th panel:* Same as previous panel but for  $\delta a$ . The vertical dashed line in the second panel is the threshold used for the binary fraction analysis in Section 3.1

extinction-corrected color  $BP - RP$  and absolute magnitude  $M_G$  for  $\sim 3.87 \times 10^6$  sources selected using the same criteria as in Equation 6 but with a distance cut  $D < 400$  pc. To remove the effects of dust reddening we use the maps of Schlegel et al. (1998) and extinction coefficients presented in Gaia Collaboration et al. (2018). Two sections of the HRD stand out immediately thanks to a strong RUWE excess indicated by shades of orange and red. These regions are known to be dominated by binary stars: the multiple-star Main Sequence that sits above the single-star MS and the white-dwarf-M-dwarf binary sequence. The clear pattern of systematic RUWE variation across the HRD as revealed by Figure 1 lends credence to the idea of using the reduced  $\chi^2$  of the astrometric fit to probe for stellar companions.

## 2.1 Amplitude of the angular perturbation $\delta\theta$

If the photocentre motion deviates from that of a single source, we can decompose the residual as  $R_i = R_i^{ss} + \delta\theta_i$ , where the  $\delta\theta_i$  represents extra perturbation to the single-source residual  $R_i^{ss}$ . We take the root mean square of  $\delta\theta_i$  assuming that the single source portion of  $\chi^2_{\nu}$  is  $\sim 1$ , that  $N \gg 5$  and dropping the cross-term, and interpret the result as the amplitude of the photocentre perturbation (in mas):

$$\delta\theta = \sqrt{\langle \delta\theta_i^2 \rangle} \approx \sigma_{AL}(G) \sqrt{\rho^2 - 1}, \quad (2)$$

Here, we have substituted the per-scan along-scan centroiding error  $\sigma_i$ , which is not available, with the mean value  $\sigma_{AL}$  as a function of source magnitude  $G$  presented in Lindegren et al. (2018, blue curve in their Figure 9). This is a robust estimate of the standard deviation of the residuals of the centroid fit from their residual analysis, not the formal error from the image parameter determination. For faint sources, i.e., those with  $G > 12$ , the difference in the two along-scan centroiding error estimates is  $< 20\%$ . Note however that for the brighter objects, the formal error can be some five times smaller than the estimate we chose to use (see Lindegren et al. 2018, for details). Note that the above derivation of  $\delta\theta$  from  $\rho$  is only valid when the binary motion causes a significant photocentre wobble, i.e., when  $\rho > 1$ .

The first panel of Figure 2 shows  $\sigma_{AL}$  used here as a function of magnitude  $G$ . Additionally we demonstrate that the single-epoch

centroiding error can also be estimated as  $0.53\sqrt{N}\sigma_{\varpi}$ , where  $\sigma_{\varpi}$  is the reported parallax error (we have checked that the bulk of the results presented here does not change if we switch between the two  $\sigma_{AL}$  estimates). The second panel of the Figure gives the distribution of  $\rho$  for a sub-set of sources in Gaia DR2 (grey thick line, see Equation 6). The distribution appears to have two parts: a peak around  $\rho \approx 1$  corresponding to single sources or sources without a measurable centroid perturbation and a tail extending to large values, corresponding to objects with appreciable centroid perturbation.

In order to estimate the overall angular photocentre perturbation corresponding to the tail of this distribution, we construct a simple model for the RUWE distribution of well-behaved single sources. We assume that the distribution of  $\rho$  for the unaffected sources is symmetric, which seems reasonable if the number of observations  $N$  is sufficiently large (the median number of observations for the sample shown in Figure 2 is  $N = 225$ )<sup>2</sup>. We take the  $\rho$  histogram and reflect the low- $\rho$  part around the peak  $\rho_{peak} = 1.012$  (thin black line in the second panel of Figure 2). We approximate this symmetric distribution as a Student's  $t$ -distribution with 13.5 degrees of freedom for the scaled variable  $(\rho - \rho_{peak})\delta\rho^{-1}$  where  $\delta\rho = 0.057$  is the width of the peak.

Using this model for the  $\rho$  distribution for single sources we compare the distribution of angular perturbation  $\delta\theta$  of the whole sample with a control sample composed of single sources only. The control sample has the size equal to the number of stars in the blue peak shown in the 2nd panel of Figure 2, or, in other words, twice the number of stars with  $\rho < \rho_{peak}$ . The control sample is constructed by pairing random  $\rho$  values drawn from the model single-source  $\rho$  distribution described above with an apparent  $G$  magnitude, which gives the corresponding centroiding error  $\sigma_{AL}(G)$ . We calculate  $\delta\theta$  using Equation 2 for both samples and compare them in the third panel of Figure 2. The red line shows the differences between the measured  $\delta\theta$  distribution (black) and the model background (single source) estimate (blue). As the red line indicates,

<sup>2</sup> Note that even for such a high overall number of observations as much as  $\sim 15\%$  more sources could be located on the right side of the peak (assuming uniform distribution of numbers of observations in the range of 150 to 300 with a median of 225).

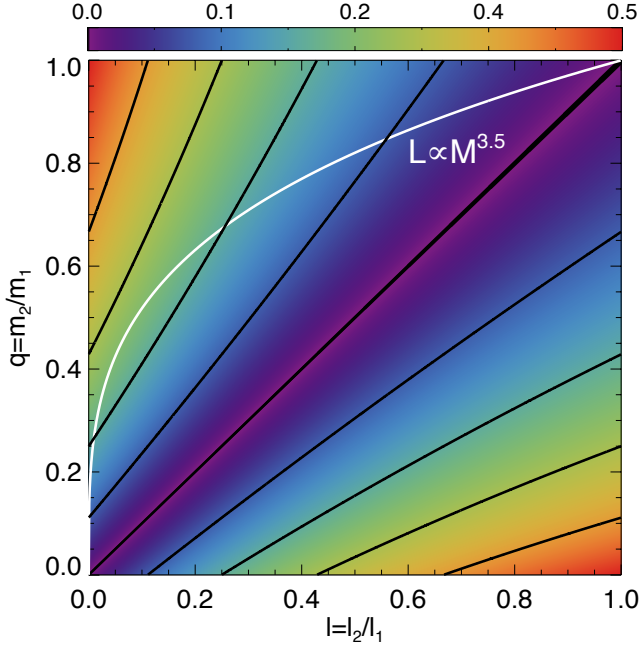


**Figure 3.** Astrometric wobble scaling factor  $\delta_{ql}$  as a function of the luminosity and the mass ratios,  $l$  ( $X$ -axis) and  $q$  ( $Y$ -axis). White curve gives an approximate behaviour for the MS stars following a power-law mass-luminosity relation. As demonstrated by the MS track, in a stellar binary the typical  $\delta_{ql} < 0.2$

photocentre wobble with amplitudes as low as  $\sim 0.1$  mas are detectable.

## 2.2 Translation to physical units

Taking the distance dependence of the centroid wobble into account, the corresponding physical displacement in AU is:

$$\frac{\delta a}{\text{AU}} = \frac{\delta \theta}{\text{mas}} \frac{D}{\text{kpc}}, \quad (3)$$

where  $D$  is the distance to the source in kpc computed as the inverse of parallax in mas. The fourth panel of Figure 2 displays the distribution of measured  $\delta a$  values as well as our estimate of the background, i.e., the contribution of sources without a detectable centroid wobble scattered to high  $\delta a$  values (blue line). The excess of objects with genuine centroid perturbation (mostly binary stars) is shown with the red line.

We emphasize that our goal is to study the overall binary statistics with RUWE and the astrometric wobble deduced from it and *not* to identify individual binary star candidates. It is obvious that at large distances small individual  $\delta \theta$  and  $\delta a$  values (corresponding to  $\rho \approx 1$ ) are not likely to be statistically significant.

Note, however, that closer to the Sun, binary systems with small separations can yield significant RUWE excess (as discussed below in Section 2.3). We refrain from identifying binary star candidates, instead, below, we present evidence for enhanced binarity for a number of distinct populations of sources. For this, we rely on two simple methods to gauge the significance of the centroid perturbation. In some cases (see e.g., Section 3.1), we use our (admittedly naive) model of single-source  $\delta a$  scatter described above. Elsewhere, we construct comparison samples with objects whose observed properties (such as apparent magnitude and color) match those in the population of interest. This allows us to claim detections of low-amplitude astrometric perturbations when it shows up as a systematic RUWE excess for the sample as a whole. Here and elsewhere in the paper we assume that the peak of RUWE distribution is centred on  $\rho \approx 1$  by design. This is tested and shown to be true (in well-populated regions of the CMD) in Figure A1 where we also discuss the behaviour of the width and the tail of the RUWE distribution. In high-density portions of the CMD, no strong variations of the RUWE distribution is reported.

An alternative approach could be taken in using astrometric excess noise (AEN) as a proxy for  $\delta \theta$ . It appears appealing for several reasons: i) AEN was designed precisely to catch additional perturbation of the stellar photocentre, ii) it does not include attitude noise and iii) it comes with an estimate of significance. However, we have decided against using AEN for the following two reasons. First, AEN “saturates” to a zero value for a large fraction of sources with determined (and reported) RUWE. For example, for the sample of stars presented in Figure 2, only approximately half of sources with  $\text{RUWE} > 1.1$ , have  $\text{AEN} > 0$ . This does not pose a problem for sources with large enough perturbations but limits our understanding of the minimally affected source (i.e. prevents the calculation of the background model described above). Second, while the distribution of RUWE is guaranteed (by design) to peak at 1 across the entire color-magnitude range of *Gaia*, an equivalent property is not ensured for AEN. It will therefore contain systematic trends as a function of color and magnitude, e.g. a strong change around  $G \sim 13$  due to the d.o.f. bug in *Gaia* DR2 (Lindegren et al. 2018). We have checked the correspondence between AEN and  $\delta \theta$  computed from RUWE and found them to be strongly correlated (see Figure A2).

## 2.3 Astrometric wobble for known binaries

What is the photocentre perturbation expected from binary motion? In the limit of unresolved binary with period much shorter than the observational baseline (such that the orbit sampled over many periods effectively ends up adding an overall jitter), we can approximate this as the difference between the center-of-light, which is the photocentre, and the center-of-mass, which will still follow single-source astrometric solution. Given a mass ratio  $q = m_2/m_1$  and a luminosity ratio  $l = l_2/l_1$ , the difference is

$$\Delta = \left\langle \left| \frac{\vec{x}_1 + l\vec{x}_2}{1+l} - \frac{\vec{x}_1 + q\vec{x}_2}{1+q} \right| \right\rangle = \frac{|q-l| \langle |\vec{x}_1 - \vec{x}_2| \rangle}{(q+1)(l+1)} \quad (4)$$

where the bracket indicates time-average and  $\vec{x}_{1,2}$  are the projected positions of the two stars. While in detail the relative vector and how it projects onto the sky plane depends on inclination and eccentricity (Penoyre et al., submitted), it will be proportional to the binary separation  $a$ . Thus, we expect the following for the physical



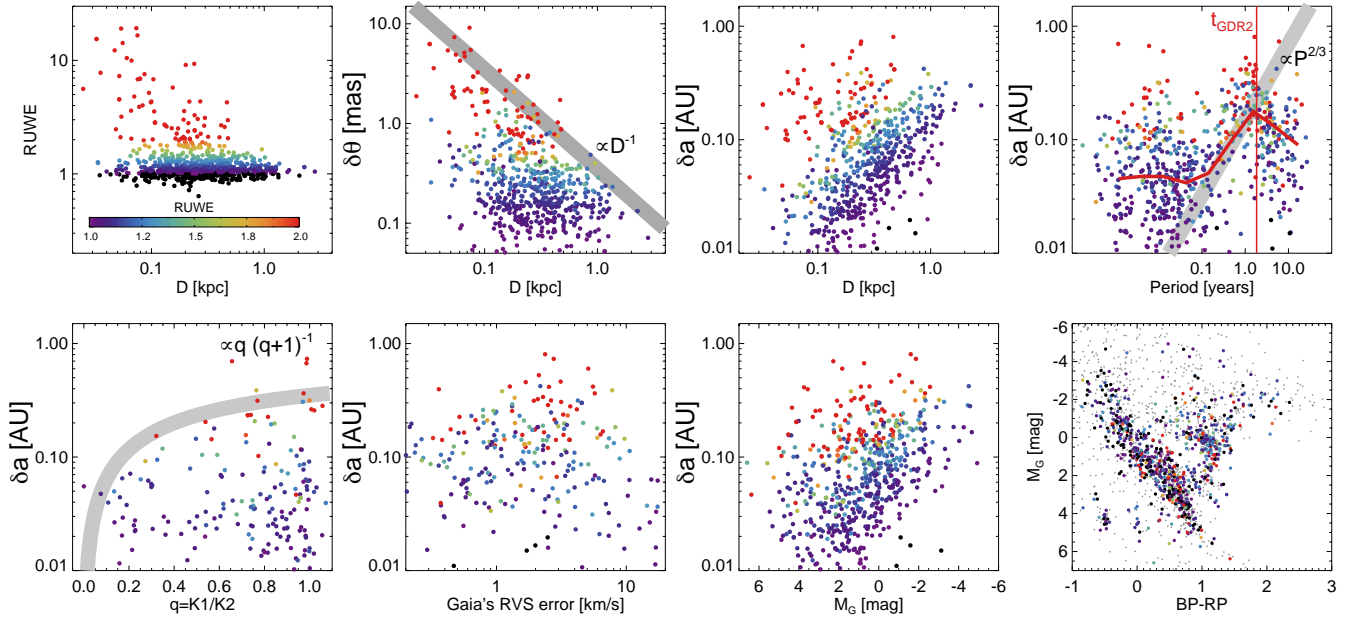


**Figure 4.** SB9 spectroscopic binaries (Pourbaix et al. 2004) as seen by *Gaia* DR2. Only 801 binaries satisfying the conditions described in the text are shown. *Top row, 1st panel:* RUWE as a function of distance to the star. The stars are color-coded according to the reported RUWE value. This color-coding is preserved in all subsequent panels. *2nd panel:* Angular displacement in mas  $\delta\theta$  as a function of distance. As shown by the grey band, the amplitude of the astrometric perturbation drops proportionally to the distance. *3rd panel:* Physical displacement in AU  $\delta a$  as a function of distance. Note that the systems of the same separation  $a$  induce astrometric perturbation of decreasing amplitude with increasing distance, thus limiting the *Gaia* DR2 sensitivity range to 2-3 kpc from the Sun. *4th panel:*  $\delta a$  as a function of the binary period in years. The red curve gives the median  $\delta a$  in a bin of period. Three regimes are apparent. For periods  $< 1$  month, the photocentre wobble for distant stars is too low for *Gaia* to detect robustly. Between 1 month and 22 months, the amplitude of the measured photocentre perturbation is proportional to the binary’s  $P^{2/3}$  in accordance with the Kepler’s 3rd law. Beyond 22 months, *Gaia*’s sensitivity drops again as this is the DR2’s baseline and only a fraction of the induced shift is detected by *Gaia*. Additionally, because of the long-term nature of the perturbation, some of the wobble can be absorbed by the astrometric solution. *Bottom row, 1st panel:*  $\delta a$  as a function of the binary mass ratio  $q$ . According to Equation 5, the amplitude of the perturbation should scale with  $q(q+1)^{-1}$  for small  $l$ . This appears to match the behaviour of the upper envelope for those SB9 systems with reported K1 and K2, as demonstrated by the grey band. *2nd panel:*  $\delta a$  as a function of the *Gaia* RVS radial velocity error. Two regimes are discernible: 1) the RV perturbation is proportional to the astrometric perturbation and 2) RV perturbation exceeds astrometric perturbation. This demonstrates the complementarity of the two signals. *3rd panel:*  $\delta a$  as a function of the system’s absolute magnitude  $M_G$ . *4th panel:* Hertzsprung-Russell (absolute magnitude as a function of color) diagram for the SB9 sources colour-coded by their RUWE value.

size of the wobble  $\delta a$ :

$$\delta a \propto \frac{a|q-l|}{(q+1)(l+1)} \equiv a\delta_{ql} \quad (5)$$

where  $\delta_{ql}$  combines the mass and luminosity ratio factors and determines the link between the actual binary separation and the measured  $\delta a$ . Note that an unresolved binary of two identical stars ( $q=l$ ) will not show any extra perturbation because the photocentre coincides with the center-of-mass. Figure 3 shows the behaviour of  $\delta_{ql}$  as a function of the luminosity and mass ratios  $l$  and  $q$ . White line gives the trajectory for a hypothetical MS population which follows a power-law mass-luminosity relation. Note that stellar  $\delta_{ql}$  does not exceed  $\delta_{ql} = 0.5$  because stellar mass is a monotonic function of stellar luminosity (note however that this assumption can be broken for stars on the RGB and the HB due to mass loss) and therefore for all luminosity ratios satisfying  $0 < l < 1$ , mass ratios will also remain within  $0 < q < 1$ . This however does not hold true for dim/dark stellar remnants such as white dwarfs, neutron stars and black holes. For such binary companions,  $l \sim 0$ , while the mass ratio can be  $q \gg 1$ . If  $q$  (or  $l$ ) is allowed to exceed 1, then  $\delta_{ql}$  can exceed 0.5 and reach values close to  $\delta_{ql} \approx 1$ . We show distributions of  $\delta_{ql}$  for binary, triple and quadruple systems composed of stars drawn from PARSEC models with different ages and metallicities in Appendix B.

Given that the typical  $\delta_{ql}$  value is  $\sim 0.1$  (as illustrated by the white line in Figure 3), Figures 2 and 3 can be used to gauge the range of the binary semi-major axes *Gaia* DR2 is sensitive to. The bulk of the  $\delta a$  residuals shown in fourth (right) panel of the Figure 2 is between 0.01 and 1, thus implying that most of the detectable binaries will have  $0.1 < a(\text{AU}) < 10$ . Note that the blue and red curves in Figure 2 are given for illustration purposes only (because they are produced by averaging over all magnitudes and distances probed). The background  $\delta a$  distribution is a strong function of distance and at low distances its contribution is strongly reduced, thus allowing for a detection of small separation binaries, i.e. those with  $\delta a \approx 0.01$  or even lower. Given the extended tails of  $\delta_{ql}$  and  $\delta a$ , detection of binary systems with larger separations, i.e.  $a > 10$  AU is possible, but for periods longer than the temporal baseline of DR2, the photocentre perturbation will become quasi-linear and thus will be absorbed into the proper motion as illustrated below in the discussion of Figure 4 (also see Penoyre et al. for detailed discussion).

### 2.3.1 Centroid wobble for SB9 binaries

Figure 4 tests whether the estimate of the photocentre wobble derived from RUWE correlates with the properties of known binary systems. For this comparison, we use the SB9 catalogue of spec-

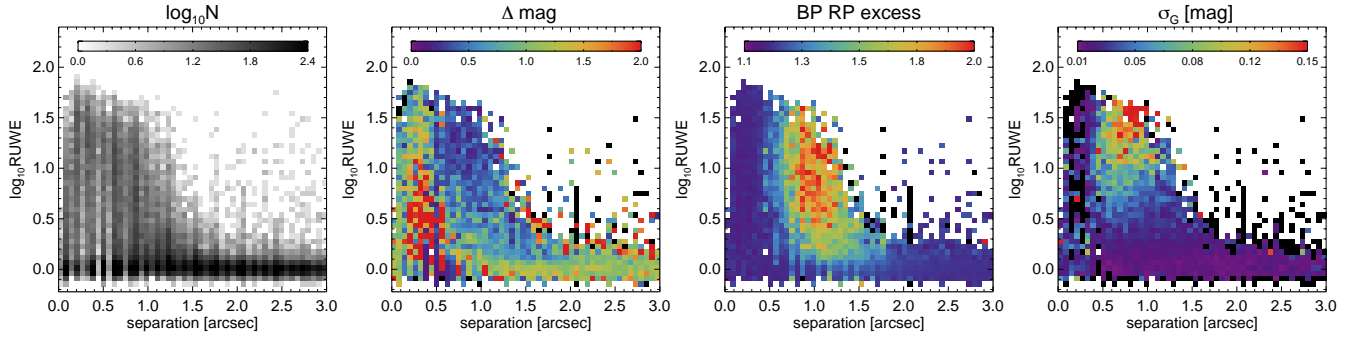


**Figure 5.** *Gaia*'s view of the double stars in the WDS catalogue (see Mason et al. 2019). *1st panel:* Logarithm of density of sources in the plane of RUWE as a function of binary separation (in arcseconds). Many of the WDS systems pile-up around  $\rho \sim 1$ . Note however a significant fraction of objects at high and extremely high values of RUWE for separations less than 1.5 arcseconds. While no correlation between RUWE and separation is observed, the upper envelope of the distribution drops with increasing separation. *2nd panel:* Median magnitude difference of the two stars as reported in WDS. Note that even systems with large magnitude differences ( $\Delta \text{mag} > 2$ ) can break *Gaia*'s astrometry. *3rd panel:* Median BP\_RP\_EXCESS\_FACTOR for WDS sources. Comparing with the second panel reveals that *Gaia* can detect excess flux when the two stars are of comparable brightness, i.e.  $\Delta \text{mag} < 0.5$ . *4th panel:* Median variability amplitude derived from error on the mean flux.

troscopic binaries (Pourbaix et al. 2004). Presented in the Figure is the subset of SB9 stars that match to a *Gaia* DR2 source within a  $1''$  aperture of their reported position. Additionally, we require

$$\begin{aligned} \text{PHOT\_BP\_RP\_EXCESS\_FACTOR} &< 3, \\ E(B - V) &< 0.5, \\ \varpi / \sigma_{\varpi} &> 15, \\ 5 < G < 20, \\ D &< 4 \text{ kpc}, \\ N_2 &= 1, \\ |M_1 - G| &< 1, \\ \text{SB9 grade} &> 1 \end{aligned}$$

here  $N_2$  is the number of *Gaia* DR2 sources within  $2''$ ,  $M_1$  is the magnitude of the first component of the binary as reported in SB9. Only 801 binary systems out of the total of 2828 recorded in SB9 survive the entirety of the above cuts.

The first panel of Figure 4 shows the amplitude of RUWE as a function of distance and demonstrates that the majority of the SB9 sources have RUWE in excess of 1 (in fact, more than 75% of those that pass the selections cuts listed above do) and that the amplitude of the RUWE excess increases with decreasing distance. Here, we simply use  $D = \varpi^{-1}$  for the distance estimate. To investigate the scaling of the astrometric perturbation with distance, it is more appropriate to convert  $\rho$  to  $\delta\theta$ . Then  $\delta\theta$  is expected to decay  $\propto D^{-1}$ , which is indeed the case as demonstrated in the second panel of the top row of Figure 4. This in turn implies that similar physical shifts (in AU) would correspond to smaller RUWE excess at larger distances (see third panel in the top row of the Figure) and thus to higher contamination. Alternatively, it can be concluded that at small distances, very tight binary systems can yield significant astrometric perturbation. For example, in the third panel of the top row in Figure 4, there are several objects with  $D < 0.1$  kpc and  $\rho > 2$  (red points) corresponding to  $\delta a < 0.1$  AU. Extrapolating to lower distances implies that few tens of parsecs away from the Sun, binaries with separation  $\delta a < 0.01$  AU can be studied using *Gaia* DR2 astrometry.

The fourth and final panel of the top row of Figure 4 displays the evolution of the astrometric wobble  $\delta a$  as a function of the binary's orbital period  $P$ . The red solid line gives the median  $\delta a$  at

given period. Three regimes are clearly discernible here. For periods shorter than 1 month, the astrometric perturbation can drop below *Gaia*'s sensitivity levels (especially for more distant sources), thus for  $P < 1$  month, the red line stays flat around  $\delta a \sim 0.05$  AU. For intermediate values of binary period, i.e. between approximately 1 month and 1 year, the photocentre perturbation, as derived from RUWE, grows  $\propto P^{2/3}$  in accordance with Equation 5 and Kepler's third law, as indicated by the thick grey band. The median  $\delta a$  curve shown by the red line changes its behaviour abruptly at  $P = 22$  months (see vertical thin line). This is the temporal baseline of *Gaia* DR2. For binary systems with periods longer than  $t_{\text{GDR2}}$ , only a small fraction of the photocentre excursion is registered by *Gaia*. Additionally, at these longer timescales, some of the centroid shift can be absorbed by the astrometric solution as an additional (spurious) component of proper motion (causing the so called proper motion anomaly, see also Penoyre et al, submitted) and/or parallax. Note that the sharp drop in sensitivity at 22 months, implies that upper end of the semi-major axis range probed is dependent on the binary mass.

Switching to the bottom row of Figure 4, the first panel gives the dependence of the astrometric wobble amplitude  $\delta a$  on the mass ratio of the binary as measured by the ratio of the velocity amplitudes of its components. The upper envelope of the distribution appears to obey Equation 5, leaving the top left corner of the Figure empty. The second panel of the bottom row compares the astrometric perturbation of a binary source to its radial velocity signature. In practice, we compare  $\delta a$  to the radial velocity error as measured by the RVS on-board *Gaia*. The two probes of binarity are highly complementary, as the RV-based methods are more sensitive to smaller separation systems where the radial velocity error (which samples the orbital velocity) reaches higher values, while the amplitude of the astrometric photocentre perturbation increases with growing separation. In the second panel of the bottom row of the Figure, two regimes are visible: at  $\sigma_{\text{RV}} < 5 \text{ km s}^{-1}$ , radial velocity error correlates with  $\delta a$ . However, the astrometric signal drops for higher RV perturbations as those, we hypothesise, are achieved by systems with small separations. The penultimate panel in the bottom row of Figure 4 shows the amplitude of the astrometric signal as a function of the source magnitude. The final (rightmost) panel in the bottom row gives the positions of the analysed SB9 sources on the HRD. This sample is dominated by the (young) MS, although

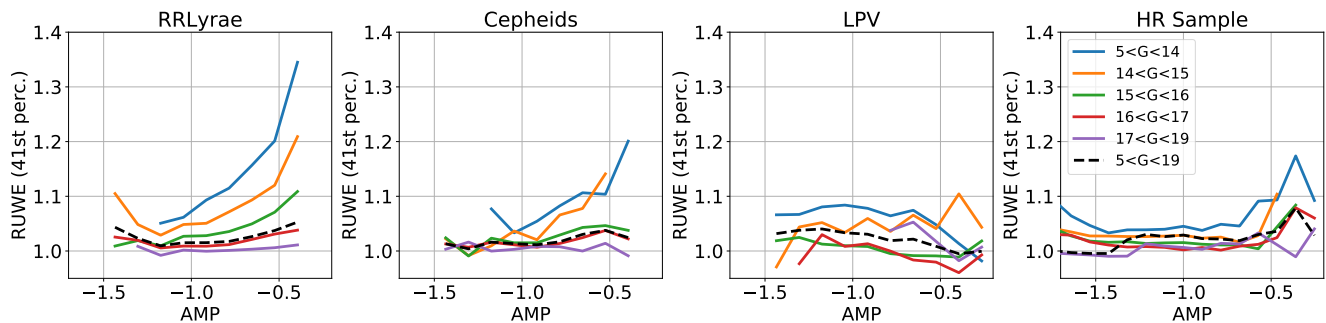


**Figure 6.** RUWE as a function of variability amplitude, estimated using Equation 2 in Belokurov et al. (2017). RR Lyrae (1st panel), Cepheids (2nd panel), LPVs (3rd panel) and stars selected using criteria specified in Equation 6 are split into 5 groups according to their apparent magnitude (colored solid lines, see inset in panel 4). For each group, we also show the overall behaviour (black dashed line). Bright RR Lyrae and Cepheids show a clear correlation between RUWE and variability amplitude.

many RGB stars are also present. Interestingly, rather rarer EHBs are also represented (see the clump at  $BP-RP \sim -0.5$  and  $M_G \sim 4$ ).

## 2.4 Other causes of RUWE excess

It is not always possible to relate the quality of the *Gaia*'s astrometric fit to the physical properties of the binary. In what follows we consider two such cases.

### 2.4.1 Marginally resolved sources

The most obvious such situation occurs when the double star is nearly resolved, i.e. the stellar image is perturbed from a single-star PSF but *Gaia* identifies and measures it as a single object. As a result, there exists a gross mismatch between the image shape and the PSF/LSF model of it, which results in a large centroiding error. The nominal “centre” of such semi-resolved binary image depends strongly on the scan angle and will oscillate wildly as a function of time<sup>3</sup>. We explore the details of this catastrophic break-down in Figure 5 which shows *Gaia*'s astrometry for sources in the Washington Double Star (WDS) catalogue (Mason et al. 2019). The first panel of the Figure shows the logarithm of the density of stars in the plane spanned by RUWE and the separation of the double star. A sharp climb-up of RUWE to extreme values is observed for separations less than  $\sim 1.5$  arcsec. However, as obvious from the Figure there is no correlation between  $\rho$  and the binary separation. As the second panel demonstrates, large RUWE values are reported for a wide range of the companion magnitude difference: at small separations, even faint companions can cause significant centroid displacement. The brighter companions can possibly be picked up as they contribute to a noticeable BP/RP excess as illustrated in the third panel of the Figure. Finally, the fourth panel shows that at separations  $> 0.5$  arcsec, semi-resolved objects start to show significant variability (as gleaned by the error of mean flux measurement). Overall, the bulk of semi-resolved double-stars can in principle be filtered out by applying cuts on BP/RP excess and variability. Note however, that double-stars with separations less than  $\sim 0.5$  arcseconds can not be identified this way. As the second panel of the

Figure illustrates, at these separations, RUWE appears to grow proportionally to the luminosity ratio. It is therefore possible that in this regime, RUWE scales similarly to that for unresolved binaries. In what follows, we do not attempt to cull potential semi-resolved double-stars (although a cut on parallax error gets rid of most of extreme RUWE cases). This should not affect the analysis presented below under the assumption that semi-resolved double-stars affect all stellar populations equally.

### 2.4.2 Variability

We also detect a tendency for RUWE to increase slightly with photometric variability as illustrated in Figure 6 for RR Lyrae, Cepheids (see Clementini et al. 2019) and Long Period Variables (see Mowlavi et al. 2018), as well as the sample of objects satisfying the cuts presented in Equation 6. The RR Lyrae stars have been selected joining the objects classified as RR Lyrae in the *Gaia* SOS (Specific Object Studies, see Clementini et al. 2019) and general variability (see Holl et al. 2018) tables. Stars in known globular clusters, dwarf satellites, Magellanic Clouds and Sagittarius stream have been removed following Iorio & Belokurov (2019). Finally, we apply quality cuts in all the three variable star catalogs filtering stars on  $|b|$ ,  $PHOT\_BP\_RP\_EXCESS\_FACTOR$  and  $E(B-V)$  as in Equation 6. The final cleaned catalogs contain 4163 Cepheids, 41317 RR Lyrae and 10016 Mira stars. The variability amplitude is estimated using equation 2 of Belokurov et al. (2017) and we checked that it nicely correlates with the peak-to-peak light curve amplitude measured by *Gaia* for a subsample of stars in our selection.

For each group of stars, individual panels of Figure 6 show the evolution of RUWE as a function of the photometric variability amplitude in 5 apparent magnitude bins (colored solid curves) as well as for the whole group (black dashed curve). The strongest signal is exhibited by the bright RR Lyrae  $5 < G < 14$ : for these, RUWE correlates strongly with the variability amplitude and can reach  $\rho \sim 1.3$  at the high end. This correlation subsides for fainter RR Lyrae, while the faintest stars with  $17 < G < 19$  do not show any connection between RUWE and variability. Similarly, RUWE values for the bright Cepheids, i.e. those with  $5 < G < 14$  and  $14 < G < 15$  appear to correlate with amplitude, but this dependence disappears for stars fainter than  $G = 15$ . Note that for (all) bright sources RUWE could be affected by the systematics in centroiding and attitude calibrations. The LPV RUWE values show no correlation with amplitude (3rd panel), with a very slight overall

<sup>3</sup> That partially resolved sources can lead to unreliable astrometry is also mentioned in the considerations on the use of *Gaia* DR2 astrometry (<https://www.cosmos.esa.int/web/gaia/dr2-known-issues>). See slide 48 of the associated presentation by Lindegren et al.

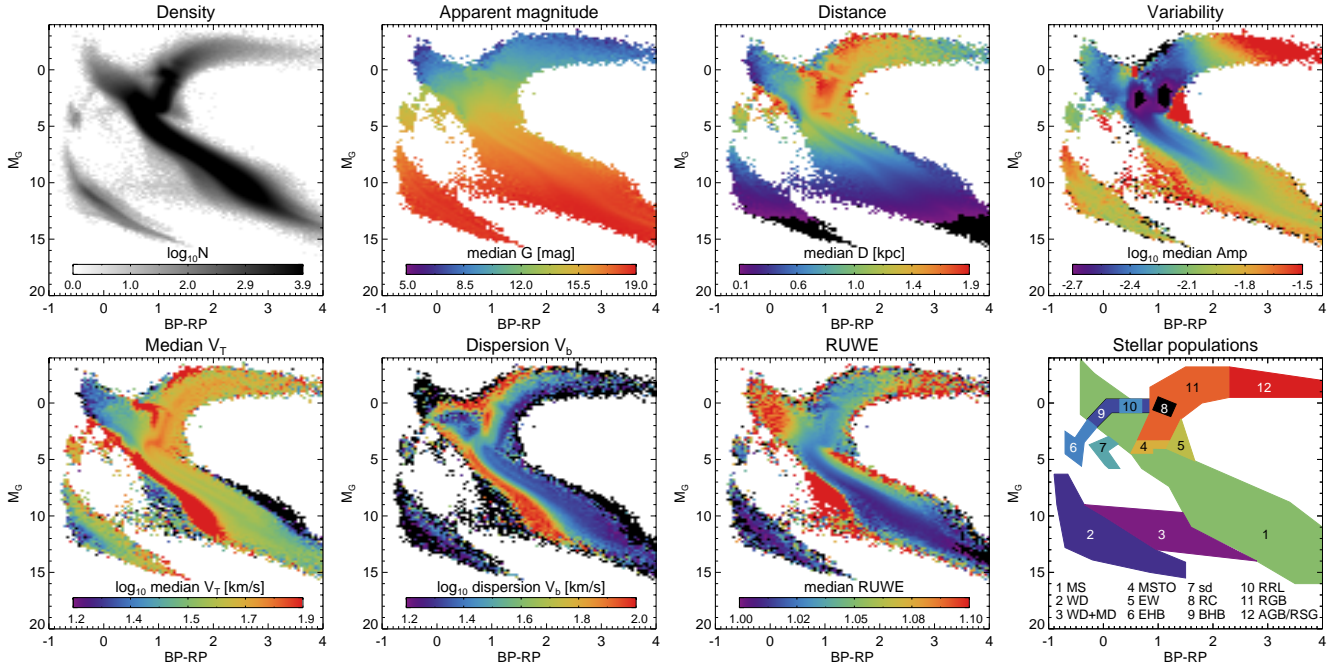


**Figure 7.** Hertzsprung-Russell Diagram for  $\sim 2.2 \times 10^7$  *Gaia* DR2 sources satisfying the selection criteria described in Section 3.1. *Top row, 1st panel:* Logarithm of source density, pixel size is  $0.053 \times 0.195$  mag. *2nd panel:* Median extinction-corrected apparent magnitude. Note a strong correlation as a function of absolute magnitude  $M_G$ . *3rd panel:* Median heliocentric distance. A pronounced gradient as a function of both colour and magnitude is visible. *4th panel:* Median variability amplitude (see Section 3.1 for details). A complicated patchwork of regions with significant variability is noticeable. *Bottom row, 1st panel:* Median heliocentric velocity  $V_T$ . The HRD space can be seen separated into thin disc (blue) thick disc (yellow) and halo (red) populations. *2nd panel:* Similar but entirely the same pattern can be seen when the HRD is colored by the dispersion in latitudinal proper motion corrected for the Solar reflex. *3rd panel:* Median RUWE. Several regions with elevated  $\rho$  are apparent. These include the photometric binary MS, B stars, and the reddest portion of the AGB. Additionally, a portion of the HRD below the MSTO exhibits elevated levels of RUWE. We argue that the astrometric solutions for these stars are completely broken. *4th panel:* Approximate stellar population boundaries.

increase for stars brighter than  $G < 15$ . The high-quality sample (Equation 6, 4th panel) shows the lowest overall values of RUWE at all  $G$ , i.e.  $\rho \sim 1$ , apart from the highest amplitude sources. The cause of the dependence of RUWE on variability as a function of magnitude for some objects may be understood by inspecting Figure 6 in Lindegren (2018). The normalization coefficient  $u_0$  is a strong function of both apparent magnitude and color, experiencing sharp changes at a several values of  $G$ , e.g.  $G \sim 13$ . A variable object will be measured by *Gaia* at a range of magnitudes (and colors) and therefore its RUWE can not be normalized using a single value of  $u_0$ . This spurious induced RUWE excess will be worse for the stars whose variability takes them across the sharp features seen in Figure 6 of Lindegren (2018). An additional contribution to the RUWE for variable stars is due to the assumption that the PSF used in the centroiding of the source images is independent of source colour and magnitude (section 2.2 in Lindegren et al. 2018). These effects make it difficult to interpret any RUWE excess for variable stars.

### 3 SOME APPLICATIONS

#### 3.1 Binary fraction across the Hertzsprung-Russell Diagram

We explore how the binary fraction evolves across the HR diagram as traced by RUWE. Figure 7 presents the distribution of  $2.2 \times 10^7$  *Gaia* sources in the space of extinction-corrected absolute magnitude  $M_G$  and colour  $BP - RP$ . These objects were selected by applying the following criteria.

$$\begin{aligned}
 & |b| > 15^\circ, \\
 & \text{PHOT\_BP\_RP\_EXCESS\_FACTOR} < 3, \\
 & E(B - V) < 0.25, \\
 & \varpi / \sigma_\varpi > 10, \\
 & \sigma_\varpi < \sigma_\varpi^{97}, \\
 & 5 < G < 19, \\
 & 0.01 < D < 3 \text{ kpc}, \\
 & N_8 = 1.
 \end{aligned} \tag{6}$$

Here  $N_8$  is the number of *Gaia* sources within an  $8''$  aperture and  $\sigma_\varpi^{97}$  is the 97th percentile of the parallax error distribution in a given (uncorrected for extinction) apparent magnitude  $G$  bin. The motivation for the  $\sigma_\varpi^{97}$  cut is to cull objects with the worst astrometric solutions, especially those whose parallaxes we can not trust (we suspect that some of these could be semi-resolved blended stars discussed in Section 2.4.1).

The first panel in the top row shows the logarithm of the HRD density distribution. Many familiar ubiquitous, as well as rare, stellar populations are readily identifiable. These are (going from faint to bright stars) the main sequence (MS, 1), the white dwarf (WD, 2) sequence, the White-dwarf-M-dwarf binary sequence (WD+MD, 3), the MS turn-off (MSTO, 4), the contact eclipsing binaries (EW, 5), the extreme horizontal branch (EHB, 6), sub-dwarfs (sd, 7), the red clump (RC, 8), the blue horizontal branch (BHB, 9), the RR Lyrae (RRL, 10), the red giant branch (RGB, 11) and the asymp-



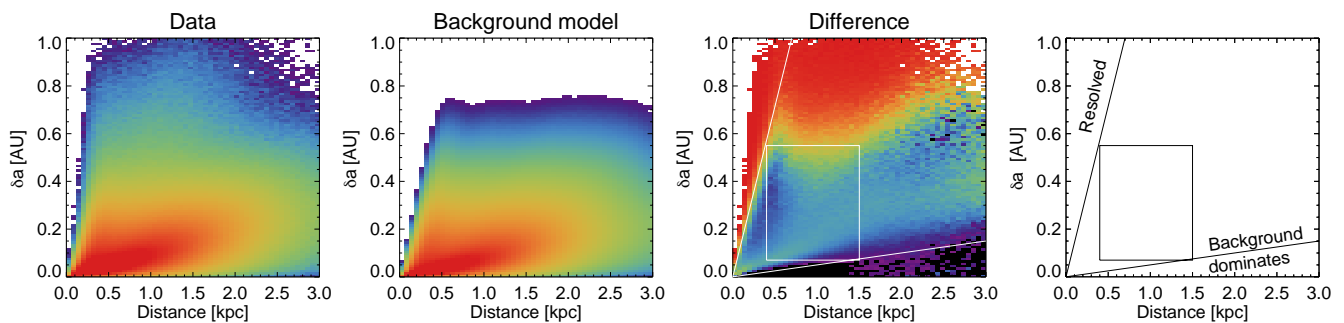


**Figure 8.** *1st panel:* Logarithm of source density in the space of centroid wobble  $\delta a$  and distance for a subset of *Gaia* DR2 objects selected using equation (6). *2nd panel:* Same as previous panel but for a mock background sample. *3rd panel:* Difference between the measured and background density distribution of  $\delta a$  as a function of distance. Rectangular box shows the selection boundaries used to study binary fraction in Section 3.1. Diagonal lines mark the regimes where i) the binary sources stop being resolved by *Gaia* and ii) the background starts to dominate as the scatter is amplified by a factor  $\propto D$ . *4th panel:* Selection boxes (see previous panel) only shown for clarity.

otic giant branch (AGB, 12). As the second panel in the top row of Figure 7 illustrates, there is a strong correlation between the position on the HR diagram and the apparent magnitude of a star. Also, given a wide range of intrinsic luminosities, stars in different portions of the HR space, reach different distances from the Sun (third panel of the top row). Given that the observed astrometric perturbation is proportional to the apparent magnitude (via  $\sigma_{AL}$ ) and inversely proportional to distance, these strong couplings may imprint significant selection biases in the distribution of RUWE across the HR space.

Many additional correlations are apparent. For example, shown in the fourth (and final) panel of the top row of Figure 7 is the median variability amplitude as gauged by the mean flux error (see Belokurov et al. 2017). Note that for this plot we convert the amplitude into magnitudes and subtract the median magnitude error in quadrature as a function of  $G$ . Here, three regions dominated by high amplitude of variability are apparent: contact eclipsing binaries (EW), RR Lyrae and long-period variables (LPV) and Mira stars. As illustrated in the first and second panels of the bottom row of the Figure, stars also cluster differently in the HR diagram depending on their kinematics. High heliocentric tangential velocity or large dispersion in the latitudinal component of the proper motion tends to pick up the thick disc and halo populations. These stars are typically older and more metal-poor than the thin disc and thus pile-up on the blue side of the MS and the RGB. Also, high tangential motion selection tends to emphasise the horizontal branch stars, typical denizens of the halo (and possibly thick disc). The third panel of the bottom row of Figure 7 shows the median RUWE in pixels of the HRD. Apart from the stars with spurious parallax measurements directly underneath the MS at  $1 < BP - RP < 1.5$ , there are three regions of the HRD where median RUWE is significantly different from  $\rho = 1$ : the AGB, the YMS and the binary (and ternary) MS. At faint magnitudes, the WD sequence stands out as the region of the HRD with the lowest fraction of stars with RUWE excess. This should not be surprising: both of the progenitors in the WD binary must have evolved away from the MS and expanded while ascending the RGB. In close systems this would result in interaction and merging. Wide double white dwarfs would not have interacted but these have periods longer than what *Gaia* DR2 is sensitive to ( $\sim 2$  years or larger). Between the WD+MD sequence and the MS there exists a region with very high RUWE values. We have investigated the properties of these stars and concluded that their parallax measurements likely suffer a strong systematic bias. Based on their proper motions, they are likely to be distant MS stars for

which *Gaia* overestimates parallax significantly. This could happen because some of these stars are partially resolved double stars (see Section 2.4.1). Additionally, some of these could be binary systems with the orbital periods close to 1 year (see the companion paper by Penoyre et al, submitted). Finally, the fourth (rightmost) panel of the bottom row presents a combination of masks marking the locations of the stellar populations mentioned above.

### 3.1.1 A binary fraction estimate

We estimate the fraction of stars in binary systems by calculating the number of objects with a centroid perturbation above a certain threshold. This ought to be done with  $\delta a$  because RUWE and  $\delta\theta$  strongly depend on the apparent magnitude and distance. Figure 8 helps to understand the sensitivity range of *Gaia* DR2. It shows the source density in the plane of centroid perturbation (in AU)  $\delta a$  as a function of distance (in kpc). The observed distribution can be compared to the model distribution of single (or unperturbed) stars shown in the second panel of the Figure. The third panel displays the density difference between the data and the background model. Two regimes are immediately apparent. At small distances, large separation binaries are resolved and therefore an empty triangular-shaped region can be seen in the left portion of all three panels. At small separations, it is progressively difficult to detect sources with statistically significant centroid perturbations at larger distances. Hence, a dark region (with negative residuals) can be seen in the bottom right of the third panel. Guided by these trends, we select a region with  $0.4 < D(\text{kpc}) < 1.5$  and  $0.07 < \delta a(\text{AU}) < 0.55$ , which we use to estimate the binary fraction. This particular range of  $\delta a$  is also beneficial as it allows us to probe the regime where the bulk of the sources lie (for the given distance bracket), compared to say  $\delta a > 0.5$  where the sensitivity is nominally higher but where very few objects exist.

Figure 9 shows the fraction of stars falling within the selection boundaries marked in the third and the fourth panels of Figure 8 for each pixel of the HRD. Note that the number of stars satisfying the  $\delta a$  and heliocentric distance cuts stated above is corrected for the background contribution, which requires an estimate of the number of unperturbed sources. The number of unperturbed sources is calculated for each pixel of HRD as twice the number of stars with  $\rho < \rho_{\text{peak}}$ , where  $\rho_{\text{peak}}$  is the same as above. For the low tangential velocity, and therefore more metal-rich and younger, stellar population shown in the top row of Figure 9 three distinct areas of elevated binary fraction are visible. They are the photometric



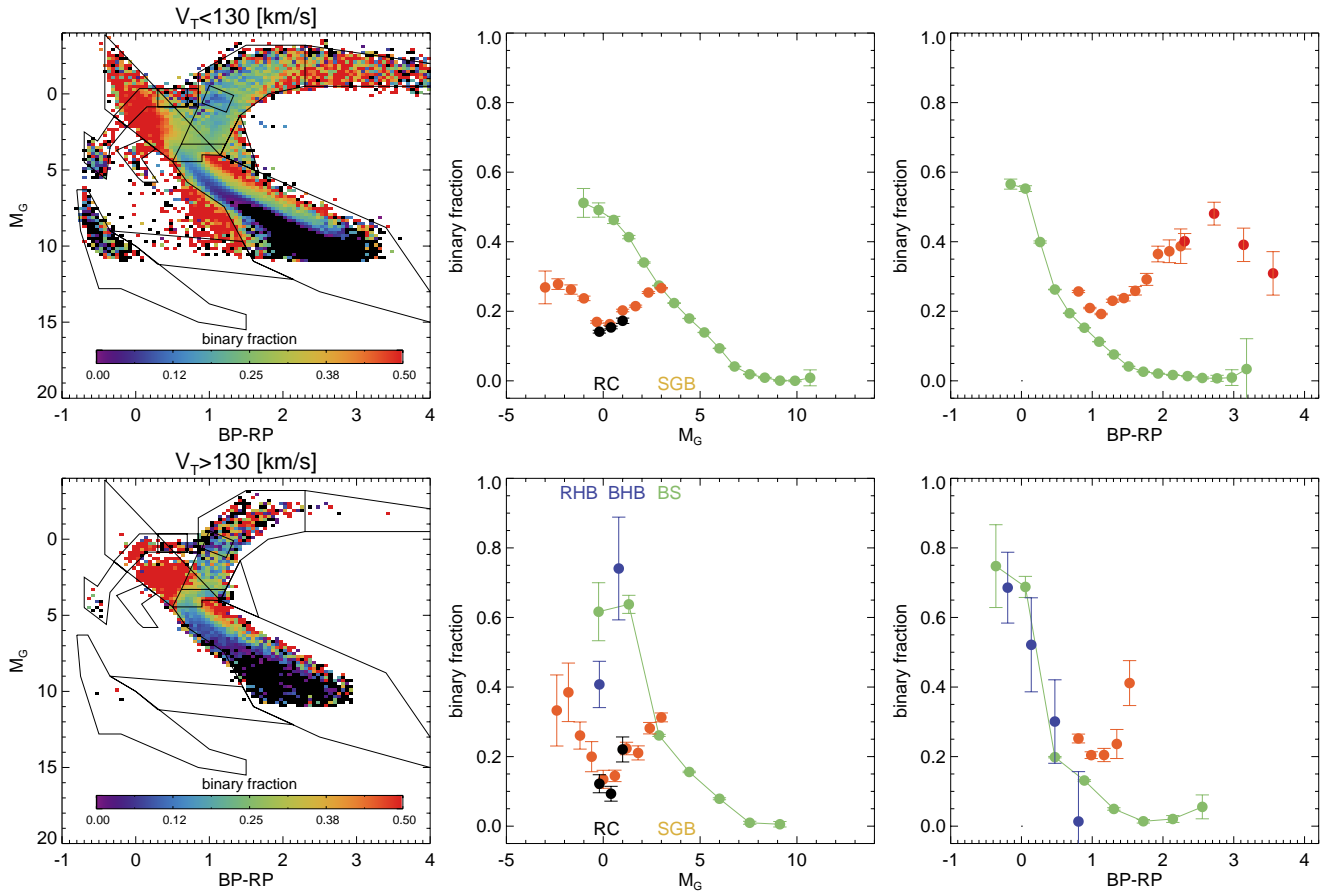


**Figure 9.** Binary fraction across the HRD. *Top:* Low heliocentric velocity sample  $V_T < 130 \text{ km s}^{-1}$ . *Bottom row:* Same as the top row but for stars with high heliocentric tangential velocity  $V_T > 130 \text{ km s}^{-1}$ . *Left column:* Ratio of the number of stars within the selection box shown in panels 3 and 4 of Figure 8 to the total number of stars in the pixel. Black lines show the same stellar population boundaries as shown in Figure 7. Several regions in the HRD show a clear excess of binary stars: i) the photometric binary (and higher multiples) sequence, ii) the young MS. On the other hand, photometric single-star MS shows low binary fraction. Binarity is also subdued on the RGB. Finally, for the high tangential velocity sample (shown in the bottom row), BS and BHB regions show a clear and strong binary fraction enhancement. *Middle column:* Background-subtracted binary fraction as a function of absolute magnitude  $M_G$ . Note i) a trend of increasing binary fraction with increasing stellar luminosity on the MS, ii) significantly lower fraction on the RGB and iii) a dip in binarity around the RC. *Right column:* Same as previous column but as a function of colour BP-RP.

binary main sequence running parallel to and above the single star MS, the young MS at  $BP - RP < 0.5$  and the AGB region. For the high tangential velocity, and therefore more metal-poor and older, stellar population shown in the lower row of the Figure, the binary fraction similarly increases at the binary MS, which is offset to the blue compared to its metal-rich counterpart shown in the top row. Both Blue Horizontal Branch stars and Blue Stragglers show highly elevated binary fractions. Along the RGB, for both slow and fast  $V_T$  stars the binary fraction remains approximately constant. In both rows, a clear drop in binarity is noticeable around the RC location. For redder giant stars, i.e. those with  $BP - RP > 2$  which end up in our AGB box, the binary fraction shows a mild increase. Perhaps, the simplest explanation of this signal is that the RUWE excess is spurious and is caused by stellar variability (as discussed in Section 2.4.2). Indeed many of the stars in this part of the HRD and Long Periodic Variables.

The middle (right) column of the Figure presents binary fraction as a function of absolute magnitude (colour) for the MS (RGB) in green (orange). Several trends are immediately visible. First, along the MS the binary fraction grows as a function of decreasing  $M_G$  and  $BP - RP$ , indicating an increase in binarity with stellar

mass. On the RGB, the binary fraction is approximately half that of the MS at similar luminosities. A region around the RC location shows a noticeable dip in binarity compared to the rest of the RGB.

Superficially, the trends in our binary fraction estimates match those reported in the literature. We see a continuous evolution where the binary fraction peaks for the high-mass MS stars, declines for the Solar-like stars and drops quickly for the MS dwarfs (c.f. Ward-Duong et al. 2015). Let us re-iterate however that the reported binary fractions should only be assessed in relative terms. These fractions are always lower (by an amount which is only known approximately) compared to the published estimates due to the selection bias introduced by design: we measure the incidence of systems with separations above a certain threshold.

### 3.2 White and Red Dwarfs

The selection discussed above is limited to distances in excess of  $D = 0.4 \text{ kpc}$  and therefore excludes intrinsically faint stars such as white dwarfs and M dwarfs. Here we analyze a smaller volume limited to  $90 < D/\text{pc} < 170$  which allows us to estimate the incidence of WD, MD and WD+MD pairs. At these distances, wide

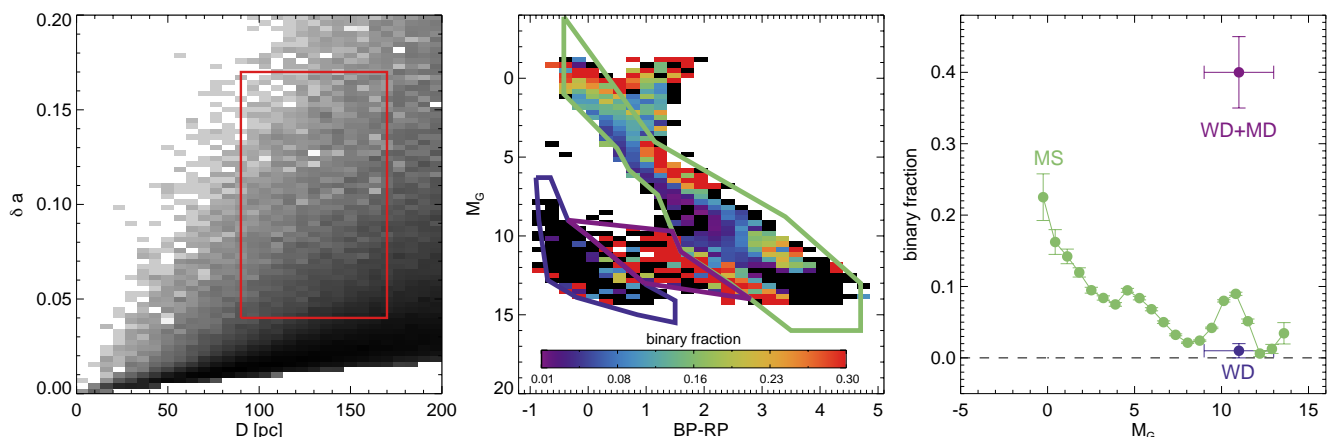


**Figure 10.** *Left:* Photocentre perturbation  $\delta a$ /AU as a function of distance (in pc) for the same sample considered in Figures 8 and 9 but closer to the Sun. Red rectangle gives the selection boundary used to compute the binary fraction shown in the next two panels. *Middle:* Fraction of stars with  $0.04 < \delta a$ /AU  $< 0.17$  amongst those with  $90 < D$ /pc  $< 170$  as a function of position on the Hertzsprung–Russell diagram. *Right:* Overall binary fraction for the MS stars as a function of absolute magnitude  $M_G$  (green). Also shown the binary fraction measurements for the double WDs and WD+MD pairs.

pairs are resolved, but conversely, *Gaia*'s astrometry is sensitive to binaries with smaller orbits, therefore we count objects with separations  $0.04 < \delta a$ /AU  $< 0.17$ .

The left panel of Figure 10 shows the background-subtracted distribution of  $\delta a$  as a function of heliocentric distance. For the stars abiding by the selection criteria specified in Equation 6 and lying in the distance range discussed above (see the boundary shown in red in the left panel) the middle panel of the Figure gives the map of the binary fraction as a function of colour and absolute magnitude. The third panel of the Figure presents binary fraction estimates for the three stellar populations highlighted in the middle panel, the MS, the WD and the WD+MD pairs. In agreement with the measurement for the more distant sample presented in the previous section the MS binary fraction increases steadily with  $M_G$  (and hence with mass). Using the local sample, we can extend the trend to  $M_G > 10$ . This reveals two wiggles in the binary fraction curve, one at  $M_G \sim 5$  and another one at  $M_G \sim 10$ . Some of the increase at  $M_G \sim 10$  is likely due to WD+MD pairs where the white dwarf companion is cool and faint enough not to change the colour of the MS companion drastically. It is unclear if the entirety of binary fraction fluctuation can be explained by the WD+MD pairs. As a population, the photometric WD+MD pairs residing in the area of the HRD between the MS and the WD sequence possess the highest binary fraction in the sample considered. Note that, obviously, nearly all objects<sup>4</sup> in this region of colour and magnitude should be binaries. Note that as above, our estimate concerns the systems in a particular range of semi-major axis sizes.

The incidence of WD+WD binaries is the lowest at  $\sim 1\%$ . This is in good agreement with the recent measurement of Toonen et al. (2017) who report the binary fraction of  $1\% - 4\%$  for their unresolved double WDs. Assuming that all objects within the WD+MD mask are binaries, the observed fraction of  $\sim 40\%$  can be used to estimate the selection bias for double WD in our sample, which gives  $2.5\%$  after correction.

<sup>4</sup> There could be some contamination from objects with spuriously large parallaxes as discussed above.

### 3.3 Blue Stragglers

The left panel in the bottom row of Figure 9 reveals a substantial population of stars between the turn-off and the horizontal branch that are likely too luminous and too hot for the typical age of the selected sample. These are the so-called Blue Lurkers or Blue Stragglers (Sandage 1953; Burbidge & Sandage 1958). According to current theories, more than one star is needed to make a Blue Straggler. In dense stellar systems, such as globular clusters, the suspiciously young-looking BSs are probably made by direct stellar collisions (Hills & Day 1976). Note that the frequency and the efficiency of such interactions can be greatly enhanced if the colliding systems are binaries to begin with (Leonard 1989; Bailyn 1995). Thus, even in star clusters, the bulk of BSs have probably come from a parent binary population (see Leigh et al. 2007; Knigge et al. 2009; Geller & Mathieu 2011). Alternatively, irrespective of its environment, a star in a binary system can be rejuvenated as a result of the mass transfer from its companion (McCrea 1964; Chen & Han 2008a,b). Finally, the third scenario invokes a parent triple system in which the Kozai-Lidov mechanism pushes the inner binary to undergo Roche-lobe overflow and possibly merge (Perets & Fabrycky 2009). It is likely that a combination of the above mechanisms is required to explain the observed properties of BSs. Note that in all three scenarios, the BSs can be either a stellar merger product or a result of a mass transfer. The latter yields a BS in a binary, while the former can be a single star.

According to Figure 9, the binary fraction in the BS region of the HRD is the highest across the entire sample. Given the possible contamination and the systematic biases associated with our simple measurement procedure, it is quite likely that we underestimate the true binary fraction amongst the BS. These could be 100% binaries. Generally, our measurements are in agreement with the earlier spectroscopic studies that found a high fraction of binaries amongst the field BSs (e.g. Preston & Sneden 2000; Carney et al. 2001, 2005; Jofré et al. 2016; Matsuno et al. 2018) and BSs in star clusters (e.g. Mathieu & Geller 2009). There has also been some progress to identify the typical companions of the BSs. Geller & Mathieu (2011) used a statistical argument to point out a particular companion type, that with the mass of  $0.5 M_\odot$ , strongly implicating a WD (and therefore a mass transfer from a giant origin). Most recently, WDs were indeed confirmed to accompany BSs in several

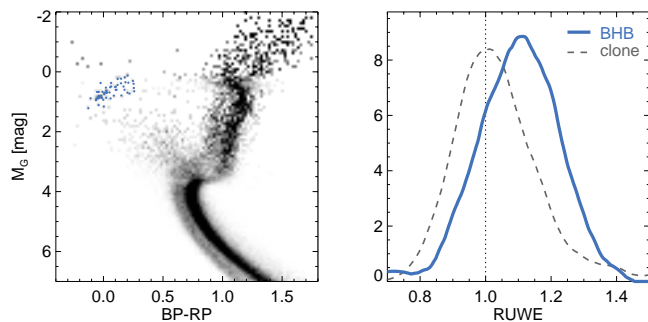


**Figure 11.** Photocentre wobble of Blue Horizontal Branch stars. *Left:* Color-Magnitude Diagram of high heliocentric tangential velocity stars (see Figure 9). BHBs stand away from the rest of the old stellar populations due to their relatively high temperatures and intrinsic luminosities. Selected BHB candidates are shown in blue. *Right:* Distribution of the RUWE values for the BHB candidates selected as shown in the left panel (solid blue) and the comparison sample (‘clone’; dashed grey). The ‘clone’ sample contains stars of marching BP – RP colour and apparent magnitude  $G$  (before extinction correction).

star clusters via detection of UV excess (Gosnell et al. 2014; Sindhu et al. 2019; Sahu et al. 2019). Taken at face value, our measurements indicate that the contribution of merged stars must be rather small if the first two formation scenarios are considered. Note however that in view of our observations mergers are not ruled out if BS originate in triples.

### 3.4 Position on HB, mass loss and binaries

Figure 9 indicates a surprisingly high binary fraction for stars on the HB. To verify whether this could possibly be due to an artefact we conduct the following simple test. We select candidate BHB stars from the sample of objects satisfying the criteria listed in Equation (6), a cut on tangential velocity  $V_T > 130 \text{ km s}^{-1}$  and a colour-magnitude selection shown in the left panel of Figure 11. For each of the 54 BHB candidates, we identify 30 clones, i.e. stars matching the BHBs in (uncorrected for dust)  $BP - RP$  colour and magnitude  $G$ . As demonstrated in the right panel of Figure 11, the RUWE distribution of the comparison (clone) sample peaks at  $\rho \approx 1$  while that of the BHB candidates is shifted towards higher RUWE, with its peak located at  $\rho \approx 1.1$ . From this test we conclude that the detected increase in binarity for the BHB stars is unlikely to have been caused by the *Gaia* systematics.

Low-mass stars (those with mass  $< 2.5 M_\odot$ ) are expected to shed significant portions of their outer envelopes as red giants (RGs) in order to touch down on the long and narrow Horizontal Branch. There they evolve by burning helium in the core surrounded by a hydrogen shell, and will slide along the HB left and right before ascending the Asymptotic Giant Branch (AGB) and disappearing from our view as white dwarfs (WDs) (see e.g. Catealan 2007, and references therein). The RGB mass loss controls the exact placement of a star on the HB and therefore governs its subsequent evolution. However, no solid theoretical explanation of the mass loss exists to date. Instead, current stellar evolution models rely on simple mass loss parameterizations (e.g. Reimers 1975; Schröder & Cuntz 2005). This lacuna in the otherwise physically-motivated stellar evolution theory is also notoriously difficult to make good through direct observations (e.g. Origlia et al. 2007; Groenewegen 2012; Origlia et al. 2014). One of the best known

applications of the RGB mass loss ansatz is the interpretation of the observed diversity of the globular cluster (GC) HBs. The HB morphology (its temperature profile) is explained by the degree to which the helium core is exposed. The GC data indicate that the primary factor responsible for the HB diversity is the cluster’s metallicity, while the age and the He abundance may act as the second and third parameters (Gratton et al. 2010). Curiously, using the same GC HB data to calibrate the mass-loss laws mentioned above, McDonald & Zijlstra (2015) find little dependence on metallicity but a relatively high mass-loss rate. This result is contradicted by Heyl et al. (2015) who show that at least in the case of 47 Tuc, the RGB mass loss is minimal, adding to the growing body of evidence that the RGB mass loss rates may be significantly overestimated (e.g. Mészáros et al. 2009). In the absence of a working theory of RGB mass loss, other scenarios facilitating mass removal have been suggested. For example, stellar fly-bys and binary interactions can provide pathways to transfer mass away from the RGB or enhance its wind (Tout & Eggleton 1988; Fusi Pecci et al. 1993; Buonanno et al. 1997; Lei et al. 2013; Pasquato et al. 2014).

### 3.5 Wide binaries and hierarchical triples

Recently, it was suggested that the *Gaia* kinematics of wide binary systems can be used as a gravity test, probing the regime of weak accelerations (Pittordis & Sutherland 2018; Hernandez et al. 2019). By examining relative velocities as a function of the binary separation, we find a substantial number of systems for which the velocity difference exceeds that of the predicted escape speed (see Pittordis & Sutherland 2019). However, this high velocity tail does not necessarily require a modification of our gravity theory. As Clarke (2019) shows, high relative velocities at large separations can be explained instead by a contribution from hierarchical triples where the smallest separation binary sub-system is unresolved by *Gaia*. For such an unresolved binary, if the luminosity ratio is not unity, the photocentre exhibits an additional excursion due to the binary’s orbital motion, biasing the relative velocity in the wide binary (in reality, a hierarchical triple). Below, we provide an empirical test of this hypothesis.

Figure 12 presents the distribution of projected relative velocities (computed using the proper motion of the binary components) as a function of separation for about 29, 500 wide binary systems in the catalogue of El-Badry & Rix (2018b). Note that only MS-MS systems are used and we require that both components are bright,  $G < 17$ , and suffer little dust extinction  $E(B - V) < 0.3$ . The first (leftmost) panel in the top row shows the whole sample, while the second and third panels display low- and high-RUWE sub-samples correspondingly. As a reference, the red solid curve gives the escape velocity for a  $1 M_\odot$  system. Note that for each binary, the highest of the two individual RUWE values is chosen. Comparing the second and third panels, it is immediately clear that high-RUWE stars achieve higher relative velocities at given separation. This is further illustrated in the fourth panel of the top row, using one-dimensional velocity distributions for a range of separations between 200 and 1500 AU (marked by the red vertical dashed lines in the second and third panels). While the relative velocity distribution of the low-RUWE stars begins to drop quickly around  $1.5 \text{ km s}^{-1}$ , the high-RUWE histogram extends out to about  $3 \text{ km s}^{-1}$ . Using equation 3 of Pittordis & Sutherland (2019), we can compute the masses of the stars in a binary and thus the corresponding circular orbit velocity  $v_c$  and the associated escape velocity  $\sqrt{2}v_c$ . The middle row of Figure 12 gives the behaviour of the relative velocity normalised by  $v_c$ . Here, the horizontal red line marks the

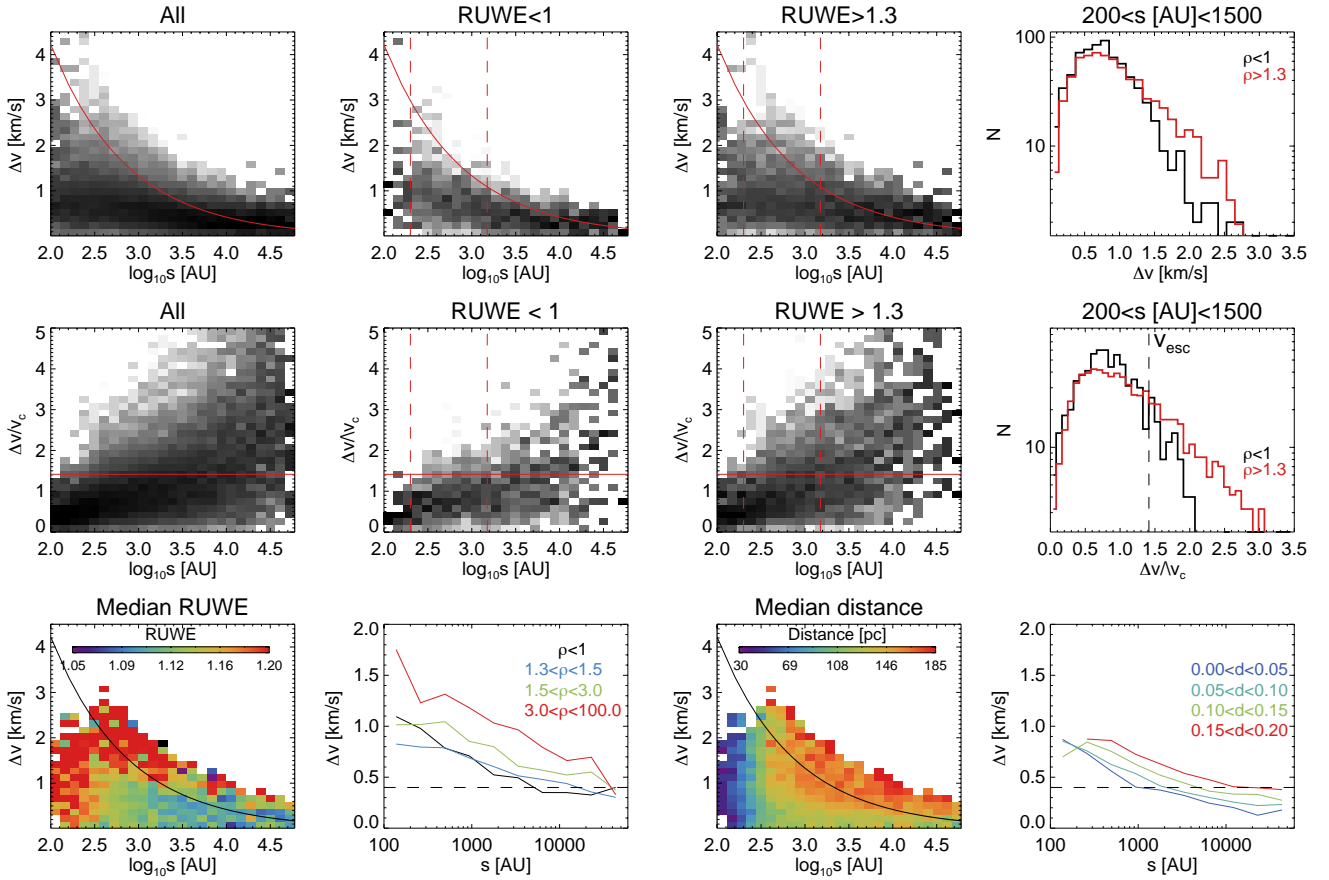


**Figure 12.**  $\sim 29,500$  wide binaries from the catalogue of El-Badry & Rix (2018b). Only systems satisfying the criteria described in Section 3.5 are shown. *Top row:* Relative projected velocity (km/s) of the pair as a function of separation (AU). *1st panel:* All systems. *2nd panel:* Systems with  $\text{RUWE} < 1$ . *3rd panel:* Systems with  $\text{RUWE} > 1.3$ . Here RUWE is the highest RUWE value in the pair. Note that binary systems with at least one star showing evidence for photocentre wobble exhibit higher relative velocities. *4th panel:* Distributions of relative tangential velocities for binary systems with separation  $200 < s(\text{AU}) < 1500$ . *Middle row:* Same as top but for relative velocity normalised by the circular velocity of the pair  $v_c$ . Note that systems with low RUWE rarely exceed the estimated escape velocity  $\sqrt{2}v_c$ , while those binaries with suspected photocentre perturbation clearly do. *Bottom row:* RUWE and distance as a function of relative velocity and separation. *1st panel:* Relative velocity as a function of separation colour-coded by median RUWE value. Note the RUWE excess at low separations and high relative velocities. *2nd panel:* Relative velocity trends for systems in four bins of RUWE. *3rd panel:* Median distance. Note a clear trend of increasing distance as a function of separation. *4th panel:* Relative velocity trends for systems in four distance bins.

escape velocity. By comparing the behaviour of the whole sample and the low- and high-RUWE subsets, we see that the bulk of the systems with relative velocity exceeding  $\sqrt{2}v_c$  are those showing strong evidence for an additional photocentre perturbation, possibly caused by an unresolved companion, in line with the hypothesis of Clarke (2019). Note that not all wide binaries with the relative velocity excess have high RUWE. Instead in these systems the period of the unresolved binary can be larger than *Gaia*'s baseline, thus yielding a well-behaved astrometric fit but noticeable proper motion anomaly (see also Penoyre et al, submitted).

The first panel in the bottom row of Figure 12 gives the distribution of RUWE in the plane of relative velocity and separation. Here, several trends are immediately noticeable. First, RUWE grows with increasing relative velocity, or rather, higher relative velocities can be achieved by unresolved small-separation binaries due to an additional photocentre wobble. Secondly, for separations  $s < 200$  AU, most of the stars have elevated RUWE. Note that the catalogue of El-Badry & Rix (2018b) is limited to 200 pc from the Sun. Therefore, stars at these separations are less than  $1''$  apart on the sky. While *Gaia* can resolve most of these systems, the quality

of the astrometric fit would most likely be affected by the presence of a bright neighbour in the close proximity. Finally, the median RUWE appears to decrease with growing separation. To understand this, it is instructive to look at the map of the median distance shown in the third panel of the bottom row. The distance distribution shows two trends. Starting at low separations, the distance increases with growing  $s$ . This is understandable because small separation binaries can only be resolved when they are nearby. There is an additional trend for  $\log_{10}(s/\text{AU}) > 3$ , where distance also appears to correlate with relative velocity. Many of the systems above the fiducial escape curve, that have been demonstrated above to have high RUWE are also typically the most distant stars in the sample. We hypothesise that this trend could possibly be due to the fact that high RUWE stars are unresolved binaries and thus are intrinsically brighter and therefore detectable to larger distances. Given these distance gradients, it is now clear why median RUWE decreases with increasing separation: the amplitude of the photocentre perturbation drops with distance as shown by Equations 2 and 3. Additionally, at larger distances, the contribution of unresolved



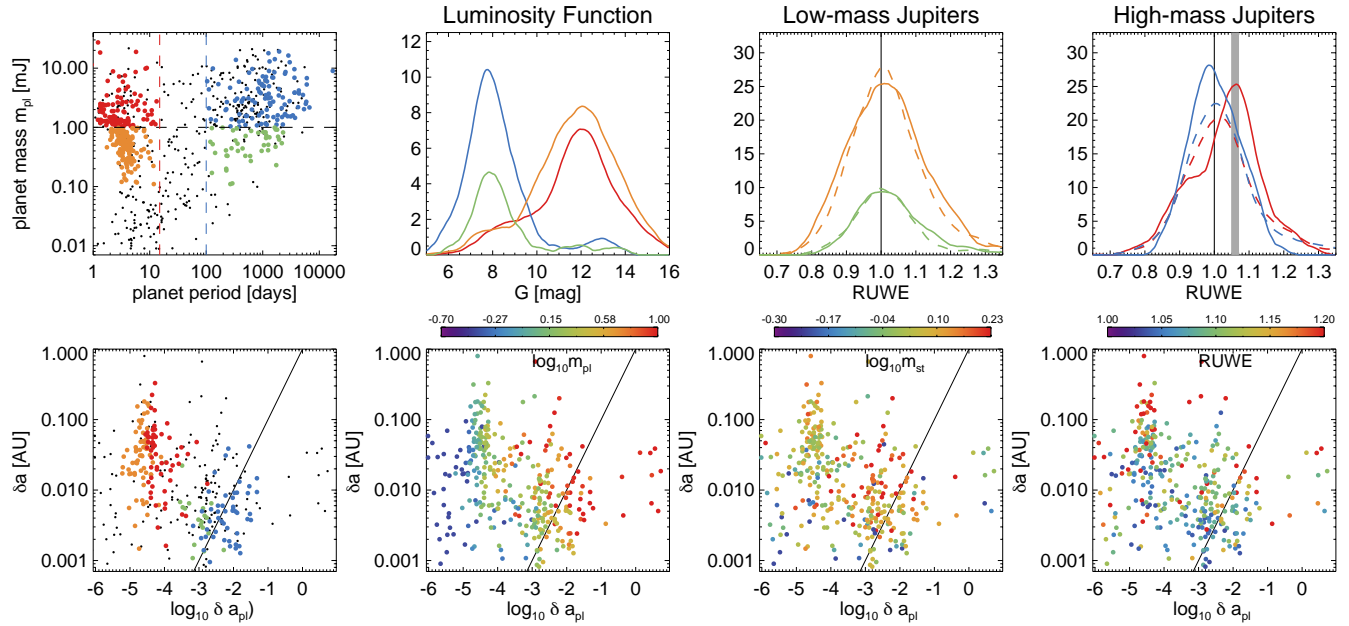


**Figure 13.** Some  $\sim 2000$  previously known exoplanet hosts as seen by Gaia (please see the main text for the sample definition). *Top row, 1st panel:* Exoplanet mass as a function of its orbital period. Colours illustrate the selection of hosts of high-mass (red) and low-mass (orange) hot Jupiters together with those of high-mass (blue) and low-mass (green) outer Jupiters. *Top row, 2nd panel:* Apparent magnitude distributions for the four groups selected as shown in the 1st panel. Note that the outer Jupiter hosts are on average much brighter than the hot Jupiter hosts. This is the consequence of the detection technique selection bias. *Top row, 3rd panel:* RUWE distributions for the low-mass Jupiters (solid lines) together with their comparison samples (dotted lines). *Top row, 4th panel:* Same as previous panel but for the high mass Jupiters. Note that the peak of the RUWE distribution for the high-mass hot Jupiters is shifted to a value higher than  $\rho = 1$ , while the peak of the RUWE distribution of the corresponding comparison population remains at 1. *Bottom row:* Photocentre wobble  $\delta a$  as a function of the predicted source displacement if it was caused by the catalogued exoplanet  $\delta a_{\text{pl}} = [m_{\text{pl}}/(m_{\text{st}} + m_{\text{pl}})]a$ . *1st:* Same colour-coding as in the 1st panel of the top row. *2nd:* Points are colour-coded according to the planet mass. *3rd:* Colour-coding according to the host mass. *4th:* Colour-coding reflects the host’s RUWE value. All of the above distributions are obtained with the optimal kernel size KDE (Epanechnikov kernel).

binaries with proper motion anomaly (and periods larger than 22 months) likely becomes more important.

Based on the analysis presented in Section 3.1, we can estimate the fraction of hierarchical triples amongst the wide binaries in the sample considered. First, RUWE values are drawn for pairs of stars from the single-source RUWE distribution following the prescription outlined in Section 2. Next the maximal RUWE for the pair is calculated to mimic the procedure we have applied to the wide-binary sample. The centroiding errors and distances are propagated to produce a distribution of  $\delta a$  for pairs of sources without statistically significant RUWEs. We subtract the resulting mock single-source  $\delta a$  distribution from the measured  $\delta a$  distribution and sum up the positive differences. In doing so, we assume that the bias owing to the binary systems being resolved at low distances and the increasing contribution of the amplified background cancel each other. We have checked that this indeed appears to be the case, because our triple fraction estimate changes very little with the distance cut applied. We report the fraction estimated for systems between 30 and 150 pc (to avoid the extremes of the biases mentioned). The sample average fraction of triples for this sample is  $\sim 40\%$ , which agrees well with the estimates in the literature (see e.g. Riddle et al. 2015) and is only slightly lower than the fraction assumed in the calculation of Clarke (2019). As explained above, binaries with periods longer than 22 months will have little RUWE excess and thus our triple fraction estimate might well be a lower bound on the true value. Going back to the original idea of testing the theory of gravity in the regime of weak interactions with wide

binaries, it is now clear that stellar multiplicity has to be carefully taken into account, as already indicated by Clarke (2019).

### 3.6 Hot Jupiter hosts

Hot Jupiters are difficult to produce at their observed separations from host stars so they are hypothesised to have migrated from larger distances either through angular momentum loss inside a remnant circumstellar disc (e.g. Goldreich & Tremaine 1980; Lin & Papaloizou 1986) or via interactions with other companions of their hosts, perhaps through the Kozai-Lidov mechanism (e.g. Wu & Murray 2003; Fabrycky & Tremaine 2007). The former pathway leads to a predominantly circular planetary orbit which is well aligned with the star’s spin axis, while the latter yields a preference for planets with misaligned and eccentric orbits. To test the importance of multi-body interactions for hot Jupiter orbital evolution, several observational experiments have been carried out recently (e.g. Knutson et al. 2014a; Wang et al. 2015; Wöllert & Brandner 2015a,b; Ngo et al. 2015a; Piskorz et al. 2015a; Ngo et al. 2016; Evans et al. 2016a). In particular, Ngo et al. (2016) and Fontanive et al. (2019) find a statistically significant excess of wide-separation (typically beyond tens of AU) companions to hot Jupiters compared to the field stars. They conclude that it is unclear how exactly such wide companions can affect the planet’s formation and/or evolution. However, most recently, Moe et al. (2019) re-assessed selection biases of the above surveys for planetary host companions and concluded that hot Jupiter hosts showed no statistically significant preference for wide companions.



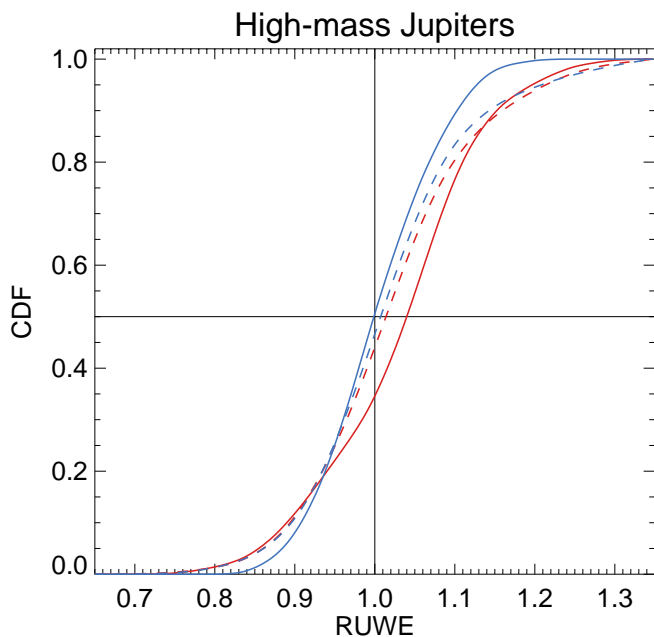


**Figure 14.** Cumulative distribution functions obtained with optimal kernel size KDE (Epanechnikov kernel) for the high-mass hot Jupiters (solid red), high-mass outer Jupiters (solid blue) and their CMD clones (dashed).

Figure 13 presents the properties of exoplanet hosts as reported by the NASA Exoplanet Archive on 6 September 2018 and cross-matched with the *Gaia* DR2 using  $1''$  aperture<sup>5</sup>. The first (left) panel in the top row of the Figure shows the exoplanet mass (in Jupiter masses) as a function of its orbital period. The host stars should have an apparent magnitude in  $5 < G < 16$  and have no neighbouring sources within  $2''$  as detected by *Gaia*. Also, the stars should be within 1 kpc from the Sun, have  $\varpi/\sigma_\varpi > 7$  and lie on the MS,  $M_G > 2.7$ . Finally, hosts need to have at least 10 comparison stars in a  $0.125 \times 0.125$  mag pixel on the apparent (BP-RP, G) colour-magnitude diagram. The combination of the above selection criteria results in a sample of 1938 exo-planetary hosts out of the 3,666 in the original sample. From this restricted dataset, we select four groups, low- and high-mass hot Jupiters (orange and red) with periods less than 15 days as well as low- and high-mass outer Jupiters, those with periods greater than 100 days (green and blue). Of these, 111 are high-mass hot Jupiters and 147 are low-mass hot Jupiters. There are also 109 high-mass outer Jupiters and 44 low-mass outer Jupiters. The second panel in the top row of Figure 13 displays the apparent magnitude distributions for the four selected exoplanet host groups. These luminosity functions reveal a strong selection bias due to a particular detection method involved. The absolute majority of outer Jupiters have so far been detected using radial velocity identification and thus their host stars are significantly brighter than those discovered by the transit method.

The third and fourth panels in the top row of Figure 13 give the RUWE distributions for the four selected exoplanet host groups together with the corresponding distributions for their comparison samples (dashed lines). The comparison samples are constructed as follows. For each of the exoplanet hosts, we identify 10 *Gaia* DR2 stars with matching colors and apparent magnitude. The low-mass

Jupiter hosts (for the planets both near and far from the host) exhibit RUWE distributions indistinguishable from those of their comparison samples (see the third panel in the top row of the Figure). The high-mass samples, in particular that of the hot Jupiters, show small but clear deviations from their comparison sets that are worth discussing. As revealed by the blue line, the high-mass outer Jupiter hosts have slightly lower RUWE values overall, and are missing the low-amplitude tail of high RUWEs. This could be due to the fact that only the most well-behaved stars are used for the radial velocity exoplanet detection. On the other hand, the mode of the high-mass hot Jupiter distribution is shifted off  $\rho = 1$  towards larger  $\chi^2_\nu$  values, i.e. the bulk of the hot Jupiter hosts show a small but systematic RUWE excess. The simplest interpretation is that these systems harbour an additional, probably low-mass and/or distant, stellar or sub-stellar component, which causes the photocentre to wobble. A grey vertical band marks the median RUWE value for 13 hosts with known companions within  $1.1''$ , namely: HAT-P-14, HAT-P-8, HD 68988, HD 86081, WASP-36, WASP-3, XO-5, HAT-P-24, HAT-P-30, HAT-P-33, HD 109749, WASP-48 and WASP-76 (see Knutson et al. 2014b; Ngo et al. 2015b; Piskorz et al. 2015b; Evans et al. 2016b; Bryan et al. 2016). Curiously, the median RUWE for the exoplanet hosts with known low-luminosity and small-separation companions matches rather well the mode of the distribution of the entire hot Jupiter sub-sample.

The bottom row of Figure 13 translates RUWE into  $\delta a$ , the amplitude of the photocentre perturbation. From the first (left) panel in the bottom row, it is evident that hot Jupiter hosts attain higher amplitude perturbations compared to those of outer Jupiters. This is perhaps not surprising given that the hot Jupiter hosts are typically much further away, thus the apparent angular astrometric wobble is scaled up by a higher typical distance. The horizontal axis in all four panels of the bottom row is the amplitude of the photocentre perturbation  $\delta a_{p1}$  if it were caused by the planet itself (see e.g. Perryman et al. 2014). It is immediately clear that  $\delta a$  and  $\delta a_{p1}$  are completely uncorrelated. Indeed it is the outer Jupiters that should cause a larger photocentre perturbation, because they span a similar mass range but are located at significantly larger distances from the host. Thus, we conclude that the photocentre perturbation as revealed by RUWE is not induced by the known planets. The next three panels in the bottom row give the same distribution as that shown in the first panel but color-coded by the planet mass (second panel), the host mass (the third panel) and RUWE (the fourth panel). Apart from a modest and expected sorting with the planet mass, no other correlations are apparent.

Figure 14 compares the cumulative distribution functions of the high-mass hot and outer Jupiters (solid lines) and their clone samples (dashed lines). Running a Kolmogorov-Smirnov test on the high-mass hot Jupiters and their clones, we obtain the probability of 0.03 that the two samples come from the same distribution. This probability goes down to 0.009 if we limit the host star distances to 0.5 kpc (and the number of hosts to 90). This indicates that there may indeed be a modest amount of statistical significance present in the RUWE excess of the high-mass hot Jupiters. High-mass outer Jupiters and their clones have a probability of 0.003 to have come from the same distribution, which also supports the idea that the differences we saw, i.e. evidence for selection biases favouring well-behaved stars, may be genuine (see e.g. discussion in Moe et al. 2019). For the low-mass systems, the KS test supports the hypothesis that the RUWE values for the planet hosts and their clones come from the same distribution, for the hot low-mass Jupiters with a probability of 0.38 and for the low-mass outer Jupiters with a prob-

<sup>5</sup> see <https://gaia-kepler.fun> for details

ability of 0.27. These numbers only increase if a distance cut of 0.5 kpc is applied.

#### 4 CONCLUSIONS

We have demonstrated that for stars with unresolved companions, the reduced  $\chi^2$  of a single-source astrometric fit provided as part of *Gaia* DR2 can be used to gauge the amplitude of the star's photocentre perturbation induced by the system's orbital motion. In practice, we work with the renormalized unit weight error (RUWE) or  $\rho$ , the square root of the reduced  $\chi^2$  rescaled to peak at  $\rho = 1$  across the entire colour-magnitude space observed by *Gaia*.

Using a sample of known spectroscopic binaries, we have shown that the amplitude of the angular centroid wobble drops inversely proportional to the star's distance, as expected. The photocentre displacement scaled by the source distance,  $\delta a$ , increases with the binary's separation and mass. Predictably, *Gaia*'s sensitivity to astrometric binaries is a function of distance as well as mass and luminosity ratios. We estimate that for systems within 1-2 kpc from the Sun, systems with semi-major axis size between 0.1 and 10 AU can be detected. Smaller separation binaries, i.e. those with  $\delta a/\text{AU} < 0.1$  can still be identified if they are nearby. Wider binaries, corresponding to periods longer than several years do not produce a significant RUWE excess because the centroid displacement - as observed by *Gaia* - is quasi-linear and is absorbed into the proper motion. Nonetheless, *Gaia* can pick these systems just as well, not with RUWE excess, but using the so-called proper motion anomaly instead (see Penoyre et al. for details)

We have also identified situations when the object's RUWE can increase due to factors not related to the binary orbital motion. For example, a semi-resolved double star (a genuine binary or a chance alignment) identified as a single object by *Gaia* can have an excess RUWE due to the mismatch between the model PSF and the observed image. Additionally, variable stars with large amplitudes of flux change can accumulate significant RUWE surplus. This happens by design, because the normalizing coefficient for RUWE is calculated under the assumption of constant apparent magnitude.

Taking advantage of *Gaia*'s unprecedented sensitivity, we have measured stellar binary fraction for a wide spectrum of stellar populations across the Hertzsprung–Russell diagram. In the range of semi-major axes accessible to *Gaia*, the binary fraction changes dramatically as a function of star's mass and its evolutionary phase. On the Main Sequence, binarity is at its highest for the youngest (and thus most massive) stars and drops steadily as one moves to lower mass stars, eventually reaching the level of only few percent at the bottom of the MS. We find that local Blue Stragglers and Blue Horizontal Branch stars both show high levels of binarity. The lowest incidence is observed for double white dwarfs, of which only 1% are detected to reside in unresolved binaries. Note this number needs to be corrected for the imposed selection effects and the overall double WD fraction is higher but unlikely to exceed 10%.

Analysing the astrometric properties of wide binary companions, we have measured a high occurrence rate of hierarchical triples. The inner binary sub-system is typically unresolved by *Gaia* but can be detected when it exhibits RUWE excess. Such unresolved inner binaries yield an additional contribution to the relative outer binary velocity (in agreement with Clarke 2019). Our estimate of  $\sim 40\%$  triple incidence amongst wide binaries is only a lower limit. This is because a single-source fit works well for systems with periods longer than the *Gaia* DR2 temporal baseline (see Penoyre et al.).

Finally, we have explored the astrometric behaviour of exoplanetary hosts. Typically, only low-mass stars with massive planets on wide orbits have a chance of being perturbed enough to be detected by *Gaia*. It is therefore surprising to see a hint of an excess of hot jupiter hosts with small but measureable centroid perturbations. In these systems, the planets are too close to their hosts to perturb the star's motion. We conclude therefore that, if real, this detection can be interpreted as a possible evidence for the presence of additional low-mass companions to massive hot jupiter hosts.

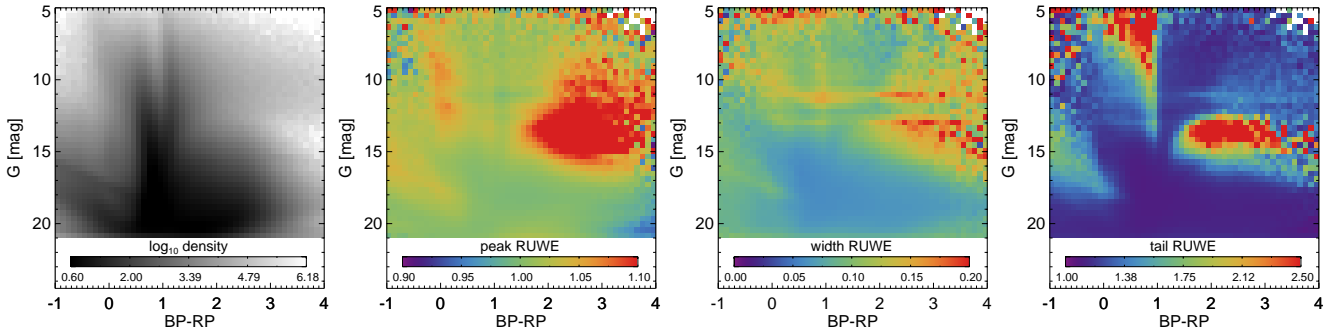
#### ACKNOWLEDGMENTS

The authors are grateful to Simon Jeffery, Floor van Leeuwen, Mark Wyatt, Annelies Mortier, Nikku Madhusudhan, Ingrid Pelisoli, Silvia Toonen and members of the Cambridge Streams Club for many illuminating discussions that helped to improve this manuscript. This research made use of data from the European Space Agency mission *Gaia* (<http://www.cosmos.esa.int/gaia>), processed by the *Gaia* Data Processing and Analysis Consortium (DPAC, <http://www.cosmos.esa.int/web/gaia/dpac/consortium>). Funding for the DPAC has been provided by national institutions, in particular the institutions participating in the *Gaia* Multilateral Agreement. This paper made use of the Whole Sky Database (wsdb) created by Sergey Koposov and maintained at the Institute of Astronomy, Cambridge with financial support from the Science & Technology Facilities Council (STFC) and the European Research Council (ERC). This work made use of the *gaia-kepler*.fun crossmatch database created by Megan Bedell. SK acknowledges the support by NSF grants AST-1813881, AST-1909584 and Heising-Simons foundation grant 2018-1030.

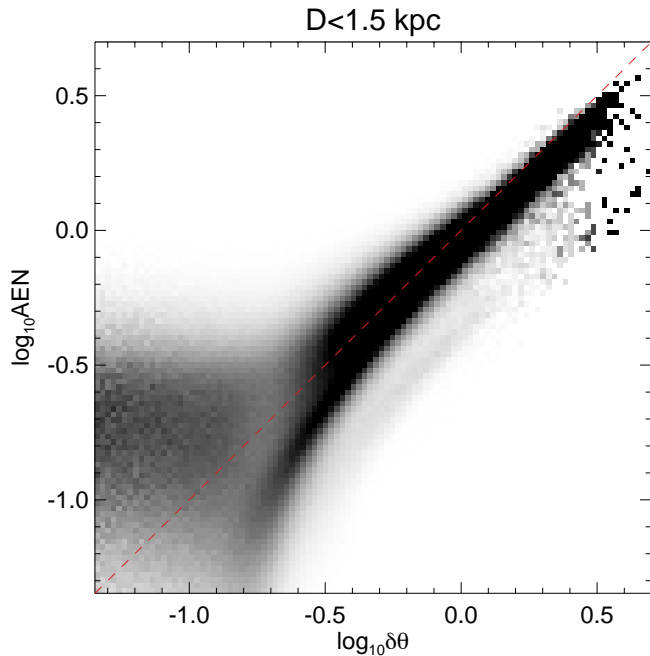
#### APPENDIX A: RUWE DISTRIBUTION ACROSS THE CMD, CONNECTION TO AEN

Figure A1 shows the properties of the RUWE distribution as a function of the position on the Color-Magnitude Diagram spanned by extinction-corrected color  $BP - RP$  and apparent magnitude  $G$  for  $\sim 2.8 \times 10^8$  sources with  $|b| > 15^\circ$ . The first panel of the Figure shows the density of the sources in the CMD space. Even though the distribution is convolved with the line-of-sight density profile, many familiar features, such as MS, RGB, WD etc, can be discerned. The second panel of the Figure gives the map of the RUWE peak - as traced by the 41st percentile (see Lindegren 2018) - which appears to stay around 1 in all of the well-populated regions of the CMD, i.e. for  $BP-RP < 0.5$ . Note additionally, a region in the red part of the CMD where the peak is shifted to at least 1.1 or slightly higher. This part of the space corresponds to a poorly populated region, in between the red giants and red dwarfs. The width of the RUWE distribution is given in the third panel of the Figure. It appears that the width does not vary dramatically as a function of color and magnitude, with a typical value of  $< 0.1$  and a pattern of deviation which appears to track that shown in the previous panel. Finally, the behaviour of the tail of the RUWE distribution (captured by the 90th percentile) can be seen in the fourth panel of the Figure.

Figure A2 demonstrates that, as expected, the angular centroid shift amplitude  $\delta\theta$  (calculated using equations 2 and 3) correlates tightly with the astrometric excess noise (AEN).



**Figure A1.** 1st panel: Logarithm of the density of sources with  $|b| > 15^\circ$  as a function of extinction-corrected color BP – RP and apparent magnitude  $G$ . The pixel size is  $0.1 \times 0.59$  mag, the total numbers of objects  $\sim 2.8 \times 10^8$ . 2nd panel: Peak of the RUWE distribution as captured by the 41st percentile (see Lindegren 2018, for details). 3rd panel: The width of the RUWE distribution (standard deviation of the RUWE distribution). 4th panel: The tail of the RUWE distribution as tracked by the 90th percentile.



**Figure A2.** Correspondence between astrometric excess noise (AEN) and the angular centroid shift amplitude  $\delta\theta$  calculated using equations 2 and 3.

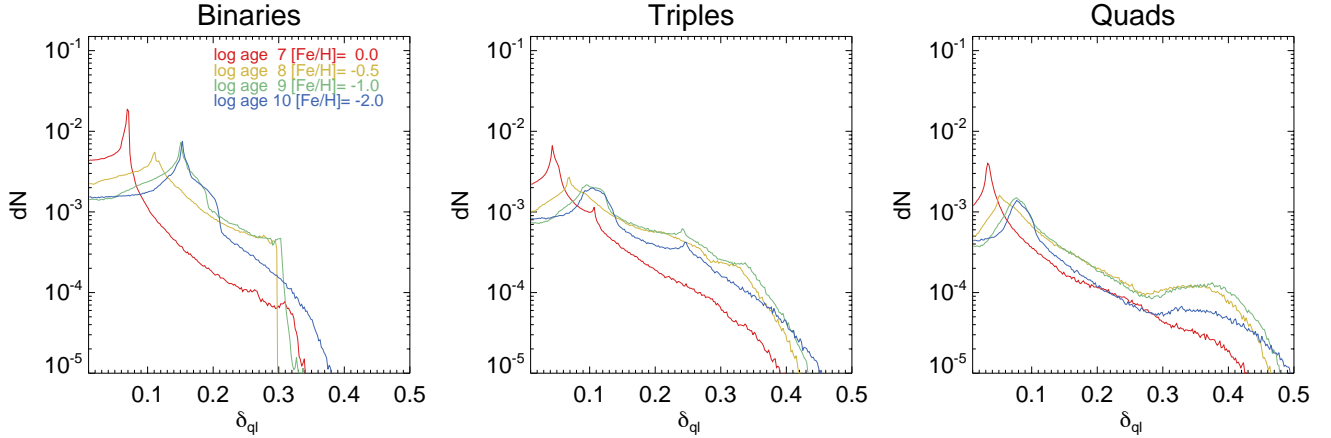
## APPENDIX B: $\delta_{qL}$ FOR MODEL STELLAR POPULATIONS

Figure B1 gives distribution of  $\delta_{qL}$  values for four PARSEC isochrones with different ages and metallicities for binaries (top), triples (center) and quadruples (bottom, these are chosen to be hierarchical systems equivalent to a binary in which one companion is a combination of three stars). As is clear from the Figure,  $\delta_{qL}$  varies depending on the stellar population and typically ranges from 0.01 to 0.2. Note that adding a compact (dark) remnant such as white dwarf, neutron star or a black hole immediately pushed  $\delta_{qL}$  high, i.e. to values close to 1 (for any of the isochrones considered). Systems of higher multiplicity (such as triples and quadruples) exhibit extended tails that stretch to higher values of  $\delta_{qL}$ , typically increasing it by a factor of 2. Higher multiples, however, can not yield  $\delta a$  values higher by an order of magnitude. We conclude therefore that the while many of the stars located in the second, low-amplitude

bump of the  $\delta a$  distribution shown in Figure 2 may well be in triples etc, the highest  $\delta a$  systems, i.e. those around  $\delta a \sim 1$ , require a dark (faint) companion, most likely a white dwarf (assuming similar distribution of semi-major axes).

## REFERENCES

- Abbott B. P., et al., 2016, Phys. Rev. Lett., 116, 061102  
 Abbott B. P., et al., 2017, ApJ, 848, L13  
 Abel T., Bryan G. L., Norman M. L., 2002, Science, 295, 93  
 Abt H. A., Levy S. G., 1976, ApJS, 30, 273  
 Andrews J. J., Chanamé J., Agüeros M. A., 2017, MNRAS, 472, 675  
 Andrews J. J., Breivik K., Chatterjee S., 2019, ApJ, 886, 68  
 Badenes C., Maoz D., 2012, ApJ, 749, L11  
 Badenes C., et al., 2018, ApJ, 854, 147  
 Baily C. D., 1995, ARA&A, 33, 133  
 Barkana R., Loeb A., 2001, Phys. Rep., 349, 125  
 Bate M. R., Bonnell I. A., Price N. M., 1995, MNRAS, 277, 362  
 Bate M. R., Bonnell I. A., Bromm V., 2003, MNRAS, 339, 577  
 Belczynski K., Kalogera V., Bulik T., 2002, ApJ, 572, 407  
 Belokurov V., Erkal D., Deason A. J., Koposov S. E., De Angeli F., Evans D. W., Fraternali F., Mackey D., 2017, MNRAS, 466, 4711  
 Berger E., 2014, ARA&A, 52, 43  
 Bessel F. W., 1844, MNRAS, 6, 136  
 Blinnikov S. I., Novikov I. D., Perevodchikova T. V., Polnarev A. G., 1984, Soviet Astronomy Letters, 10, 177  
 Brandt T. D., 2018, ApJS, 239, 31  
 Breivik K., Chatterjee S., Larson S. L., 2017, ApJ, 850, L13  
 Bryan M. L., et al., 2016, ApJ, 821, 89  
 Buonanno R., Corsi C., Bellazzini M., Ferraro F. R., Pecci F. F., 1997, AJ, 113, 706  
 Burbidge E. M., Sandage A., 1958, ApJ, 128, 174  
 Carney B. W., Latham D. W., Laird J. B., Grant C. E., Morse J. A., 2001, AJ, 122, 3419  
 Carney B. W., Latham D. W., Laird J. B., 2005, AJ, 129, 466  
 Casertano S., et al., 2008, A&A, 482, 699  
 Catelan M., 2007, in Roig F., Lopes D., eds, American Institute of Physics Conference Series Vol. 930, Graduate School in Astronomy: XI Special Courses at the National Observatory of Rio de Janeiro (XI CCE). pp 39–90 (arXiv:astro-ph/0703724), doi:10.1063/1.2790333  
 Chen X., Han Z., 2008a, MNRAS, 384, 1263  
 Chen X., Han Z., 2008b, MNRAS, 387, 1416  
 Clarke C. J., 2019, MNRAS, p. L157  
 Clementini G., et al., 2019, A&A, 622, A60  
 Duchêne G., Kraus A., 2013, ARA&A, 51, 269  
 Duquenoay A., Mayor M., 1991, A&A, 500, 337  
 El-Badry K., Rix H.-W., 2018a, MNRAS, 480, 4884



**Figure B1.** Astrometric shift scaling factor  $\delta_{qi}$  for different stellar population in binaries (top), triples (center) and quadruples (bottom). To produce  $\delta_{qi}$  distribution we use PARSEC isochrones with ages and metallicities shown in the top right corner of the top panel. Stellar masses and luminosities are drawn from the corresponding mass function. Triples (quadruples) are assumed to be in a hierarchical configuration equivalent to a binary where one component is a binary (triple) itself. Note that shapes of the distributions depend on the properties of the stellar population considered, e.g. for young metal-rich stars (red curve), a typical values of  $\delta_{qi} \sim 0.05$ . Higher multiplicity systems can achieve higher values of  $\delta_{qi}$ , typically by a factor of 2 to 4.

- El-Badry K., Rix H.-W., 2018b, MNRAS, 480, 4884  
 El-Badry K., et al., 2018, MNRAS, 476, 528  
 Evans D. F., et al., 2016a, A&A, 589, A58  
 Evans D. F., Southworth J., Smalley B., 2016b, ApJ, 833, L19  
 Fabrycky D., Tremaine S., 2007, ApJ, 669, 1298  
 Fontanive C., Rice K., Bonavita M., Lopez E., Mužić K., Biller B., 2019, MNRAS, 485, 4967  
 Fusi Pecci F., Ferraro F. R., Bellazzini M., Djorgovski S., Piotto G., Buonanno R., 1993, AJ, 105, 1145  
 Gaia Collaboration et al., 2016, A&A, 595, A1  
 Gaia Collaboration et al., 2018, A&A, 616, A10  
 Garmany C. D., Conti P. S., Massey P., 1980, ApJ, 242, 1063  
 Geller A. M., Mathieu R. D., 2011, Nature, 478, 356  
 Goldreich P., Tremaine S., 1980, ApJ, 241, 425  
 Gosnell N. M., Mathieu R. D., Geller A. M., Sills A., Leigh N., Knigge C., 2014, ApJ, 783, L8  
 Gratton R. G., Carretta E., Bragaglia A., Lucatello S., D'Orazi V., 2010, A&A, 517, A81  
 Groenewegen M. A. T., 2012, A&A, 540, A32  
 Heger A., Woosley S. E., 2002, ApJ, 567, 532  
 Heggie D. C., 1975, MNRAS, 173, 729  
 Hernandez X., Cortés R. A. M., Allen C., Scarpa R., 2019, International Journal of Modern Physics D, 28, 1950101  
 Hettinger T., Badenes C., Strader J., Bickerton S. J., Beers T. C., 2015, ApJ, 806, L2  
 Heyl J., Kalirai J., Richer H. B., Marigo P., Antolini E., Goldsbury R., Parada J., 2015, ApJ, 810, 127  
 Hills J. G., Day C. A., 1976, Astrophys. Lett., 17, 87  
 Holl B., et al., 2018, A&A, 618, A30  
 Iben I. J., Tutukov A. V., 1984, ApJS, 54, 335  
 Iorio G., Belokurov V., 2019, MNRAS, 482, 3868  
 Jofré P., et al., 2016, A&A, 595, A60  
 Kervella P., Arenou F., Mignard F., Thévenin F., 2019a, A&A, 623, A72  
 Kervella P., et al., 2019b, A&A, 623, A116  
 Kinugawa T., Yamaguchi M. S., 2018, arXiv e-prints, p. arXiv:1810.09721  
 Knigge C., Leigh N., Sills A., 2009, Nature, 457, 288  
 Knutson H. A., et al., 2014a, ApJ, 785, 126  
 Knutson H. A., et al., 2014b, ApJ, 785, 126  
 Lattanzi M. G., Spagna A., Sozzetti A., Casertano S., 1997, in Bonnet R. M., et al., eds, ESA Special Publication Vol. 402, Hipparcos - Venice '97. pp 755–760 (arXiv:astro-ph/9707019)  
 Lei Z. X., Chen X. F., Zhang F. H., Han Z., 2013, A&A, 549, A145  
 Leigh N., Sills A., Knigge C., 2007, ApJ, 661, 210  
 Leonard P. J. T., 1989, AJ, 98, 217  
 Lin D. N. C., Papaloizou J., 1986, ApJ, 309, 846  
 Lindgren L., 2018, Re-normalising the astrometric chi-square in Gaia DR2, GAIA-C3-TN-LU-LL-124, [http://www.rssd.esa.int/doc\\_fetch.php?id=3757412](http://www.rssd.esa.int/doc_fetch.php?id=3757412)  
 Lindgren L., et al., 2018, A&A, 616, A2  
 Lippincott S. L., 1955, AJ, 60, 379  
 Luyten W. J., 1971, Ap&SS, 11, 49  
 Maoz D., Mannucci F., Nelemans G., 2014, ARA&A, 52, 107  
 Mashian N., Loeb A., 2017, MNRAS, 470, 2611  
 Mason B. D., Wycoff G. L., Hartkopf W. I., Douglass G. G., Worley C. E., 2019, VizieR Online Data Catalog, p. B/wds  
 Mathieu R. D., Geller A. M., 2009, Nature, 462, 1032  
 Matsuno T., Yong D., Aoki W., Ishigaki M. N., 2018, ApJ, 860, 49  
 McCrea W. H., 1964, MNRAS, 128, 147  
 McDonald I., Zijlstra A. A., 2015, MNRAS, 448, 502  
 McKee C. F., Ostriker E. C., 2007, ARA&A, 45, 565  
 Merle T., et al., 2020, arXiv e-prints, p. arXiv:2002.02275  
 Mészáros S., Avrett E. H., Dupree A. K., 2009, AJ, 138, 615  
 Moe M., Di Stefano R., 2017, ApJS, 230, 15  
 Moe M., Kratter K. M., Badenes C., 2019, ApJ, 875, 61  
 Mowlavi N., et al., 2018, A&A, 618, A58  
 Narayan R., Paczynski B., Piran T., 1992, ApJ, 395, L83  
 Ngo H., et al., 2015a, ApJ, 800, 138  
 Ngo H., et al., 2015b, ApJ, 800, 138  
 Ngo H., et al., 2016, ApJ, 827, 8  
 Oh S., Price-Whelan A. M., Hogg D. W., Morton T. D., Spergel D. N., 2017, AJ, 153, 257  
 Origlia L., Rood R. T., Fabbri S., Ferraro F. R., Fusi Pecci F., Rich R. M., 2007, ApJ, 667, L85  
 Origlia L., Ferraro F. R., Fabbri S., Fusi Pecci F., Dalessandro E., Rich R. M., Valenti E., 2014, A&A, 564, A136  
 Pasquato M., de Luca A., Raimondo G., Carini R., Moraghan A., Chung C., Brocato E., Lee Y.-W., 2014, ApJ, 789, 28  
 Perets H. B., Fabrycky D. C., 2009, ApJ, 697, 1048  
 Perryman M. A. C., et al., 1997, A&A, 500, 501  
 Perryman M. A. C., et al., 2001, A&A, 369, 339  
 Perryman M., Hartman J., Bakos G. Á., Lindgren L., 2014, ApJ, 797, 14  
 Piskorz D., Knutson H. A., Ngo H., Muirhead P. S., Batygin K., Crepp J. R., Hinkley S., Morton T. D., 2015a, ApJ, 814, 148  
 Piskorz D., Knutson H. A., Ngo H., Muirhead P. S., Batygin K., Crepp J. R., Hinkley S., Morton T. D., 2015b, ApJ, 814, 148  
 Pittordis C., Sutherland W., 2018, MNRAS, 480, 1778

- Pittordis C., Sutherland W., 2019, *MNRAS*, 488, 4740  
Podsiadlowski P., Hsu J. J. L., Joss P. C., Ross R. R., 1993, *Nature*, 364, 509  
Pourbaix D., et al., 2004, *A&A*, 424, 727  
Preston G. W., Sneden C., 2000, *AJ*, 120, 1014  
Price-Whelan A. M., Goodman J., 2018, *ApJ*, 867, 5  
Price-Whelan A. M., et al., 2018, *AJ*, 156, 18  
Price-Whelan A. M., et al., 2020, arXiv e-prints, p. arXiv:2002.00014  
Raghavan D., et al., 2010, *ApJS*, 190, 1  
Reimers D., 1975, *Memoires of the Societe Royale des Sciences de Liege*, 8, 369  
Reuyl D., 1936, *AJ*, 45, 133  
Riddle R. L., et al., 2015, *ApJ*, 799, 4  
Sahu S., et al., 2019, *ApJ*, 876, 34  
Sana H., et al., 2012, *Science*, 337, 444  
Sandage A. R., 1953, *AJ*, 58, 61  
Schlegel D. J., Finkbeiner D. P., Davis M., 1998, *ApJ*, 500, 525  
Schröder K. P., Cuntz M., 2005, *ApJ*, 630, L73  
Sindhu N., et al., 2019, *ApJ*, 882, 43  
Smartt S. J., Eldridge J. J., Crockett R. M., Maund J. R., 2009, *MNRAS*, 395, 1409  
Smith N., Li W., Filippenko A. V., Chornock R., 2011, *MNRAS*, 412, 1522  
Sozzetti A., Casertano S., Lattanzi M. G., Spagna A., 2001, *A&A*, 373, L21  
Stacy A., Greif T. H., Bromm V., 2010, *MNRAS*, 403, 45  
Stanway E. R., Eldridge J. J., Becker G. D., 2016, *MNRAS*, 456, 485  
Toonen S., Hollands M., Gänsicke B. T., Boekholt T., 2017, *A&A*, 602, A16  
Tout C. A., Eggleton P. P., 1988, *MNRAS*, 231, 823  
Tutukov A. V., Yungelson L. R., 1981, *Nauchnye Informatsii*, 49, 3  
Wang J., Fischer D. A., Horch E. P., Xie J.-W., 2015, *ApJ*, 806, 248  
Ward-Duong K., et al., 2015, *MNRAS*, 449, 2618  
Webbink R. F., 1984, *ApJ*, 277, 355  
Whelan J., Iben Icko J., 1973, *ApJ*, 186, 1007  
Wöllert M., Brandner W., 2015a, *A&A*, 579, A129  
Wöllert M., Brandner W., 2015b, *A&A*, 579, A129  
Wu Y., Murray N., 2003, *ApJ*, 589, 605  
Yalinewich A., Beniamini P., Hotokezaka K., Zhu W., 2018, *MNRAS*, 481, 930  
Yamaguchi M. S., Kawanaka N., Bulik T., Piran T., 2018, *ApJ*, 861, 21  
van de Kamp P., 1975, *ARA&A*, 13, 295